

Recombination of localized quasiparticles in disordered superconductors

Steven A. H. de Rooij,^{1,2,*} Remko Fermin,^{3,4} Kevin Kouwenhoven,^{1,2} Tonny Coppens,¹ Vignesh Murugesan,¹ David J. Thoen,¹ Jan Aarts,⁴ Jochem J. A. Baselmans,^{1,2} and Pieter J. de Visser¹

¹*SRON - Netherlands Institute for Space Research,
Niels Bohrweg 4, 2333 CA Leiden, The Netherlands*

²*Faculty of Electrical Engineering, Mathematics and Computer Science,
Delft University of Technology, Mekelweg 4, 2628 CD Delft, the Netherlands*

³*Department of Materials Science and Metallurgy, University of Cambridge,
27 Charles Babbage Rd, Cambridge CB3 0FS, United Kingdom*

⁴*Huygens-Kamerlingh Onnes Laboratory, Leiden University, 2300 RA Leiden, The Netherlands*

Disordered superconductors offer new impedance regimes for quantum circuits, enable a pathway to protected qubits and improve superconducting single photon detectors due to their high kinetic inductance and sheet resistance. However, the relaxation of quasiparticles, which cause decoherence and microwave loss, is drastically affected by disorder, which is still not understood. We address this issue by measuring the quasiparticle relaxation time in a disordered β -Ta film, which we pattern as the inductor of a microwave resonator. We observe that the quasiparticle relaxation time is governed by the phonon scattering time and is independent on the phononic environment, which is in stark contrast to the relaxation of quasiparticles in ordered superconductors. We explain these observations in terms of the recombination of localized quasiparticles that first delocalize via phonon scattering. We analyse quasiparticle relaxation measurements on superconductors with different degrees of disorder and conclude that this phenomenon is inherent to disordered superconductors.

Disordered superconductors have a high resistance in their normal state, leading to a competition between electronic localization effects and the global phase coherence of superconductivity. A large amount of disorder can induce electronic granularity, pre-formed Cooper-pairs, ultimately causing a superconductor-to-insulator phase transition [4, 5].

Localization effects weaken the superfluid stiffness, thereby increasing the kinetic inductance (L_k) of the superconductor. This enables new regimes in high impedance quantum circuits and the development of protected qubits [6], as well as highly non-linear elements for parametric amplification [7]. For superconducting single photon detectors [8, 9], the high normal state resistance of disordered superconductors increases the broadband photon absorption efficiency [10, 11] and photon responsivity [12, 13].

Quasiparticles, the elementary excitations in a superconductor, play a central role in these applications. In quantum circuits, quasiparticles cause decoherence and microwave loss. Considerable efforts have been made to mitigate excess quasiparticles [14–18] and to explain the non-vanishing quasiparticle density at low temperatures [1, 19–21]. For superconducting radiation detectors, the relaxation of photon-generated quasiparticles dictates the detector performance [22].

As disorder increases, the relaxation time at low temperatures becomes shorter [23]. In contrast, quasiparticle relaxation times on the order of seconds have been measured in granular Al, which is highly disordered due to oxidized grain boundaries [24]. Furthermore, the microwave loss typically increases with L_k [25], which hinders the use of disordered superconductors in quantum

circuits. These observations suggest that disorder affects quasiparticle relaxation, but the underlying mechanisms remain poorly understood.

We demonstrate in this Article that localization effects govern the relaxation of quasiparticles in disordered superconductors. Disorder induces local gap inhomogeneities that serve as localization sites where quasiparticles rapidly recombine. Consequently, the relaxation process is not dominated by quasiparticle recombination, as in ordered superconductors (Fig. 1(c)), but rather by quasiparticle delocalization via phonon scattering (Fig. 1(d)). This leads to a shorter relaxation time with a weaker temperature dependence than in the absence of localization effects [26, 27]. Such a short relaxation time will help to mitigate excess quasiparticles in quantum circuits [14]. On the other hand, the localization of equilibrium quasiparticles may induce additional microwave loss [24].

RESULTS

Fluctuation measurements

We measure the quasiparticle relaxation time (τ) and density (n_{qp}) in a disordered β -Ta film [29], which is patterned as the inductor in a microwave resonator. The device is shown in Fig. 1(a) and the film parameters are given in Table I. This β -Ta film is disordered as the Ioffe-Regel parameter, $k_F l$, is close to one, with k_F the Fermi wave number and l the electronic mean free path. We therefore expect localization effects to

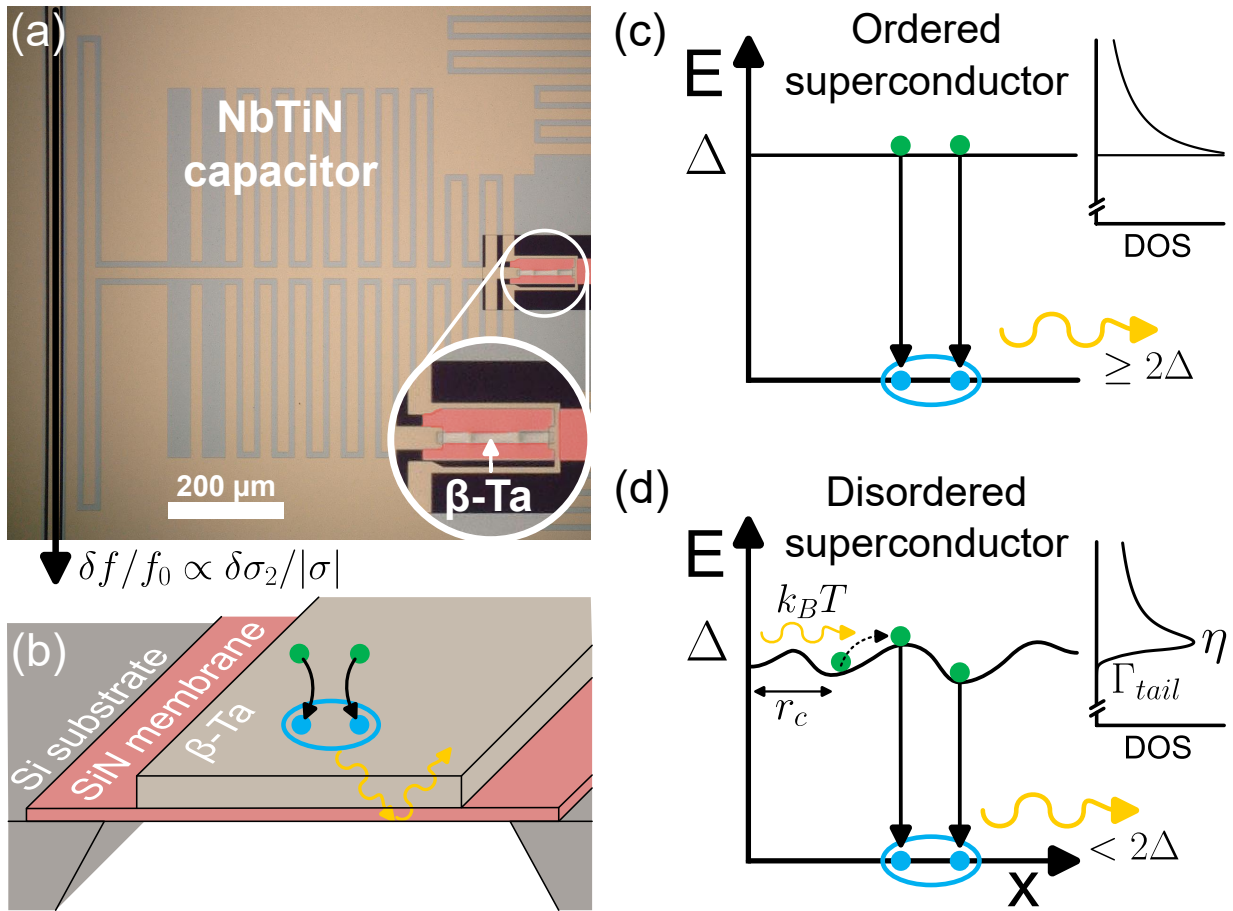


Fig. 1. **Quasiparticle fluctuation measurement and the inferred effect of disorder on quasiparticle recombination.** (a): Micrograph of the microwave resonator consisting of a NbTiN capacitor and β -Ta inductor on a membrane, which is highlighted in red. Inside the white circle the figure is two times enlarged. We measure fluctuations in resonance frequency (δf), which are proportional to complex conductivity fluctuations ($\delta\sigma_2$). (b): Sketch of the β -Ta inductor on the membrane. When two quasiparticles (green) recombine into a Cooper-pair (blue), a phonon is emitted (yellow curly arrow). A change in the number of quasiparticles or Cooper-pairs changes σ_2 , which we measure. The emitted phonon is trapped by the membrane, as indicated. (c): Sketch of traditional quasiparticle recombination with emission of a phonon with energy $\geq 2\Delta$, which can subsequently break a Cooper-pair. The BCS density of state (DOS) is sketched to the right, which has the same energy y-axis. (d): Sketch of quasiparticle recombination in disordered superconductors, which is the main finding of this work. Disorder can suppress the gap locally, inducing quasiparticle localization at a typical length scale of $r_c \sim \xi$ [1]. Quasiparticles delocalize via thermal phonon scattering, after which they recombine fast within a neighbouring localization site. This emits a phonon with less than 2Δ energy, which is very unlikely to break a Cooper-pair, eliminating the phonon trapping effect. To the right, the position-averaged DOS is sketched with a broadened coherence peak, parametrised by η , and a sub-gap tail consisting of localized states, parametrised by Γ_{tail} [2, 3].

become important. Moreover, ql is much smaller than unity, with q the phonon wave number of a phonon with energy 2Δ , which is the superconducting gap energy. This means the film is disordered with respect to electron-phonon interactions [27]. The characterization of the film is outlined in the Methods section.

We cool the resonators to bath temperatures ranging from 20 mK to 300 mK. For each bath temperature, we drive the resonator at its resonance frequency and measure time streams of the complex microwave transmission in a homodyne setup (see Methods). From that, we extract the Power Spectral Density (PSD) of the

fluctuations in σ_2 , $S_{\delta\sigma_2/|\sigma|}(\omega)$, where $\sigma = \sigma_1 - i\sigma_2$ is the complex conductivity. This is equivalent to measuring the resonator frequency noise. These fluctuations are characterised by a Lorentzian spectrum [30], as is visible in the measured PSDs in Extended Data Fig. 1. We fit a Lorentzian spectrum and extract the variance, s^2 , and relaxation time, τ , as described in the Methods section. The measured τ and s^2 are shown in Fig. 2(a) and (b). For higher and lower bath temperatures than shown in Fig. 2, the quasiparticle fluctuations were obscured by other noise sources such as $1/f$ and amplifier noise.

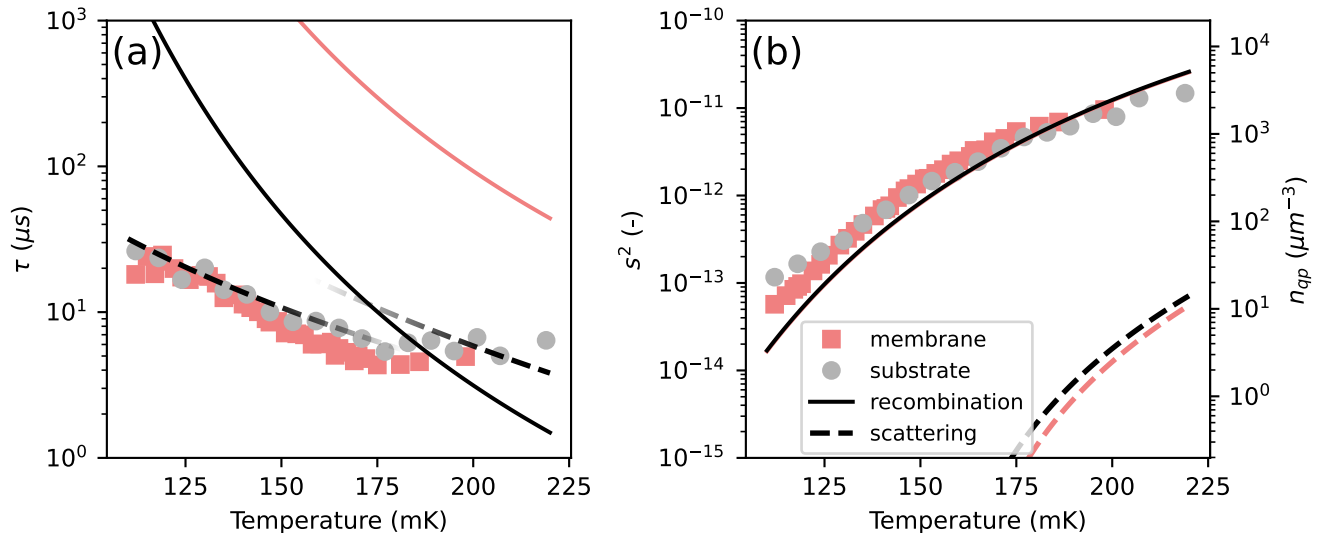


Fig. 2. **Measured relaxation time and variance compared with quasiparticle fluctuation theory.** The grey circles and red squares are determined from a fit to the measured fluctuation spectra (Extended Data Fig. 1), which gives the relaxation time (a) and variance (b) of the quasiparticle fluctuation. The red squares are for the inductor on a SiN membrane (see Fig. 1(b)) and the grey circles on a SiN/Si solid substrate, as indicated by the legend. Error bars from statistical fit errors are smaller than the data points. The dashed lines in (a) are calculations for electron-phonon scattering time, Eq. (3), which is 2D for $T < 165$ mK [28] and 3D for higher temperatures [27]. The dashed lines in (b) are the variance of quasiparticle fluctuations for scattering events. The solid lines are for recombination. The red solid line in (a) includes the expected increase in relaxation time due to phonon trapping by the membrane (Fig. 1(b)). These curves are calculated with the parameters in Extended Data Table I without fit parameters. The right axis in (b) gives the quasiparticle density corresponding to the variance of recombination events (the solid line).

Phonon scattering limited quasiparticle relaxation

We compare these measured values to the theory for quasiparticle relaxation. At low temperatures, $k_B T \ll \Delta$ with T the bath temperature and k_B the Boltzmann constant, τ is dominated by electron-phonon interactions, because n_{qp} is low compared to the normal state carrier density [26]. As a check, we compared the electron-electron and electron-phonon interaction times [31] and find that the electron-phonon interaction dominates, as outlined in the Supplementary Section 1. There are two inelastic electron-phonon processes that contribute to the relaxation of quasiparticles: *recombination* and *scattering*. In an ordered superconductor ($ql \gg 1$) and at low temperatures ($k_B T \ll 2\Delta$), recombination dominates the quasiparticle relaxation, as the typical energy of a recombination event (2Δ) is much larger than that of a scattering event ($k_B T$) [26].

During a recombination event, two quasiparticles recombine into a Cooper-pair and emit a phonon with energy $\Omega \geq 2\Delta$, as illustrated in Fig. 1(c). Quasiparticle generation is the same process, but time-reversed. The recombination time, τ_{rec} , is proportional to $1/n_{qp}$, which

exponentially decreases with temperature, i.e. [26, 27]

$$\tau_{rec}(T) = \tau_0^{rec} \sqrt{\frac{T}{T_c}} e^{-\Delta/k_B T}. \quad (1)$$

T_c is the critical temperature and τ_0^{rec} is a proportionality constant that does not depend on temperature, but does depend on disorder and dimensionality (see Methods). In our experiment, we probe the entire inductor volume and therefore measure the relaxation of an ensemble of quasiparticles. The bulk recombination time is given by [32],

$$\tau_{rec}^* = \tau_{rec}(1 + \tau_{esc}/\tau_{pb})/2, \quad (2)$$

where τ_{esc} is the escape time and τ_{pb} is the pair-breaking time of a 2Δ phonon. The last division by two in Eq. (2) describes the pair-wise nature of recombination. The factor in parenthesis is the *phonon trapping factor* and takes into account that the emitted 2Δ -phonon can subsequently break another pair. We estimate it to be 2.0 for β -Ta on a SiN substrate from the acoustic mismatch theory set out in Ref. [33, 34]. Using the separately measured parameters of the film (Extended Data Table I), which are independently measured without fitting to the data, we obtain the solid black line in Fig. 2(a). Details on the calculation of the curves

in Fig. 2 are presented in Supplementary Section 1.

We tune τ_{esc} experimentally by suspending the β -Ta inductor on a membrane, which is shown in Fig. 1(b). Via a simple geometric calculation (Supplementary Section 1), we estimate that the membrane results in an increase of τ_{esc} by factor 58 compared to the substrate case. That would increase τ_{rec}^* by a factor 29, which is shown in Fig. 2(a) as the red solid line.

An ordered superconductor, like Al and α -Ta, follows the predictions of quasiparticle recombination time including the increased relaxation time on membrane [23, 35], while we observe here that a disordered superconductor clearly does not follow those predictions.

The dashed lines in Fig. 2(a) are for quasiparticle-phonon scattering. During a scattering event, a quasiparticle absorbs or emits a thermal phonon. The relaxation time related to scattering, τ_{scat} , is proportional to the phonon occupation and therefore follows a power law versus temperature,

$$\tau_{scat}(T) = \tau_0^{scat} \left(\frac{T}{T_c} \right)^{-n}, \quad (3)$$

with $2 \leq n \leq 9/2$. n and τ_0^{scat} depend on disorder and the electron and phonon dimensionality [26–28, 36]. In our film, thermal phonons are 2D for $T \lesssim 165$ mK and 3D for higher temperatures. This changes the exponent n from 9/2 in 3D [27] to 7/2 in 2D [28]. Using the parameters from Extended Data Table I results in the dashed lines in Fig. 2(a). We divide Eq. (3) by a factor 2 in Fig. 2(a) to account for pair-wise recombination after the phonon scattering event, similar to Eq. (2).

The measured quasiparticle relaxation time in this disordered superconductor clearly follows the power-law temperature dependence of τ_{scat} and is not influenced by phonon trapping. This the main result of this article and is in sharp contrast to ordered superconductors, such as Al and α -Ta [23, 35].

Verification of quasiparticle generation-recombination fluctuations

To confirm that these results do not originate from the σ_2 -fluctuations of phonon scattering directly, we also compare the measured variance to the calculated variance of quasiparticle generation-recombination and scattering fluctuations in σ_2 . This is shown in Fig. 2(b). The solid line gives the generation-recombination variance, which is given by $s^2 = (n_{qp}/V)(d(\sigma_2/|\sigma|)/dn_{qp})^2$ [30], where V is the β -Ta volume and the factor in parentheses is the responsivity of the complex conductivity to changes in the quasiparticle density. This variance is equal for the membrane and substrate case, because it does not depend on phonon trapping. The responsivity factor is

approximately constant with temperature (< 2 % deviation in our measurement regime) and known from theory [37, 38], which allows us to directly measure the quasiparticle density from the variance. The right axis of Fig. 2(d) gives the quasiparticle density corresponding to the variance.

The dashed lines in Fig. 2(b) give the variance for scattering interactions. It is orders of magnitude lower than the variance for recombination events, because the energy difference of a scattering event is much less than that of a recombination event, $k_B T \ll \Delta$. The variance of the fluctuations clearly corresponds to the recombination of thermal quasiparticles [30]. We attribute the small deviation from the thermal line at low temperatures to microwave readout power effects [19].

We performed the same analysis to the measured dissipative fluctuations, $\delta\sigma_1$, which are shown in Extended Data Fig. 2. The results are very similar to Fig. 2. This shows that we measure quasiparticle recombination events [30, 39].

To summarize the above, we observe that the quasiparticle relaxation in this disordered film is dominated by quasiparticle recombination, but the relaxation time is governed by the phonon scattering time and is not affected by phonon trapping. This is in sharp contrast to ordered superconductors [35].

Recombination of localized quasiparticles

We can explain these observations by the localization of quasiparticles. Within a localization site quasiparticles recombine fast as they relax to the same location [1, 41]. However, a localized quasiparticle requires delocalization in order to recombine with another quasiparticle, which happens via electron-phonon scattering (Fig. 1(d)). This is relatively slow in a disordered ($ql \ll 1$) metal [42] and therefore limits the recombination process. This explains that the relaxation time is governed by the scattering time (Fig. 2(a)). The quasiparticle subsequently recombines with a localized quasiparticle, emitting a phonon with an energy below 2Δ (Fig. 1(d)). The density of localized states with $E < \Delta$ is very low (inset of Fig. 1(d)), so the chance of breaking a Cooper-pair is negligible [41]. In other words, τ_{pb} of phonons with $\Omega < 2\Delta$ is very long and Eq. (2) reduces to $\tau_{rec}^* = \tau_{rec}$. That explains why enhanced phonon trapping by the membrane does not alter the relaxation time.

A possible origin of these localized states is local gap variations induced by disorder. This is described by the theory of Refs. [2, 43], which extends the Larkin-Ovchinnikov inhomogeneous pairing theory [3]. Such gap variations have been measured in highly disordered TiN [44]. The effect of inhomogeneous pairing on the

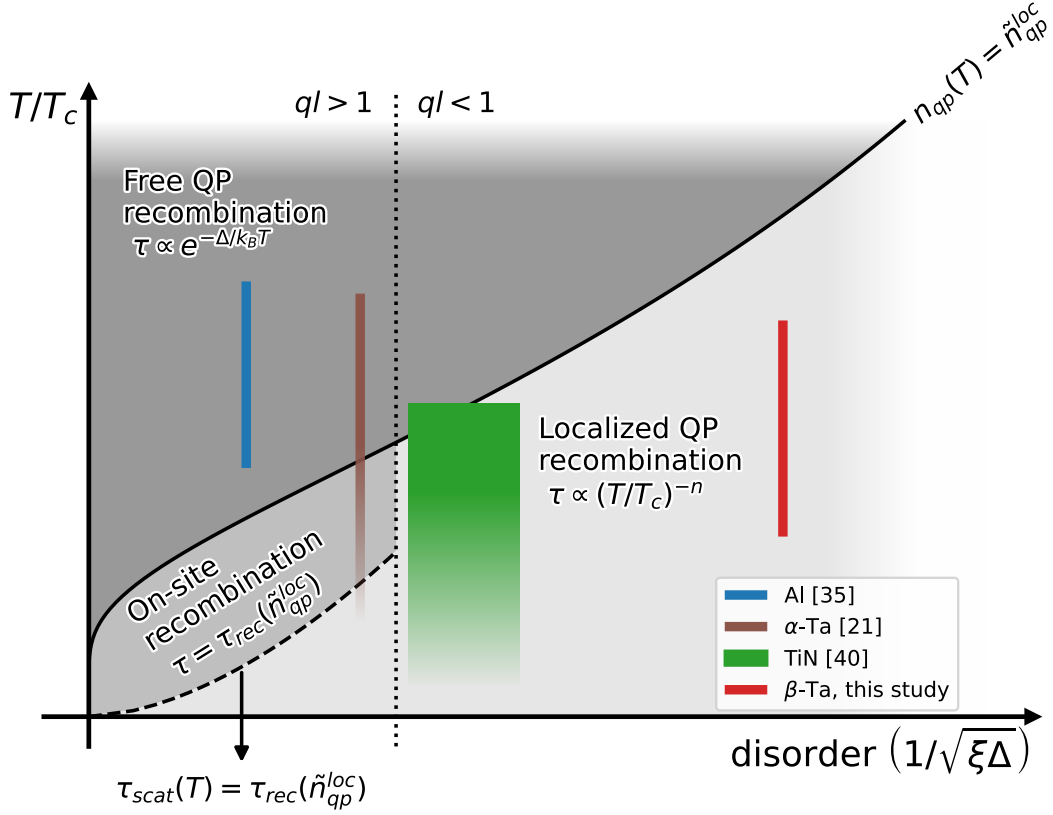


Fig. 3. **Different regimes of quasiparticle recombination as a function of temperature and disorder.** Each regime (indicated in a shade of grey) is characterised by a different temperature dependence of the quasiparticle (QP) relaxation time. The x-axis is chosen such that the dotted vertical line, $ql = 1$ for 2Δ phonons, is approximately on the same point for different superconductors. For simplicity, we take ql for 2Δ phonons only in this sketch, such that on the right side of the $ql = 1$ dashed line both recombination and scattering interactions are disordered. The solid line gives the values at which the thermal quasiparticle number equals the number of localized quasiparticle states $\tilde{n}_{qp}^{loc} = 3/(4\pi\xi^3)$. Below this solid line, all quasiparticles will therefore localize and recombine on-site. Below the dashed line and for $ql < 1$, the scattering time, Eq. (3), is longer than the recombination time, Eq. (1), at a quasiparticle density equal to \tilde{n}_{qp}^{loc} , i.e. $\tau_{rec}(\tilde{n}_{qp}^{loc})$ [26, 27]. Therefore, delocalization via phonon scattering limits quasiparticle recombination (Fig. 1(d)) in that regime, which is indicated in light grey. The coloured areas give the experimental conditions of Refs. [23, 35, 40] and Fig. 2. The fade at lower temperatures for Refs. [23, 40] are added because these are measurements via a pulsed excitation, which does not give information on the quasiparticle temperature. The recombination regimes are consistent with the observed temperature dependence of the relaxation time in the respective experiments.

density of states is two-fold: (1) the coherence peak is broadened with a pair-breaking parameter η , which is equivalent to the Abrikosov-Gor'kov description of magnetic impurities [45], and (2) the density of states acquires an exponential subgap tail of localized states, characterized by Γ_{tail} . This is sketched in the inset of Fig. 1(d). The values of η and Γ_{tail} depend on the strength of the local gap variations.

Because the thickness of our β -Ta film is on the order of the coherence length, ξ (see Methods), finite thickness effects dominate the broadening of the coherence peak and we estimate a depairing parameter of $\eta_{3D} \approx 2.9 \times 10^{-5}$ [2]. To estimate Γ_{tail} , we consider our film quasi-2D, in which case Coulomb-enhanced mesoscopic fluctuations give $\Gamma_{tail}/\Delta \approx 1.5 \times 10^{-4}$ [2]. Quasiparticle states in

this subgap tail overlap and quasiparticles in these states will recombine fast. The effective localization radius at which this process stops can be estimated from Γ_{tail} and η and is on the order of ξ [1]. With the values of η_{3D} and Γ_{tail} mentioned above, $r_c \approx 2.4\xi \approx 44$ nm. This gives a density of localized quasiparticle states of $\tilde{n}_{qp}^{loc} \approx 3/(4\pi r_c^3) \approx 2.7 \times 10^3 \mu\text{m}^{-3}$. Comparing this number to the right axis of Fig. 2(b) we conclude that the thermally generated quasiparticles localize due to gap variations for temperatures $T < 180$ mK. This leads to the situation in Fig. 1(d).

DISCUSSION

Following the same line of reasoning, we expect to see the same phenomenology in other disordered superconductors. Indeed, a weak temperature dependence of the quasiparticle relaxation time is also observed in TiN for different levels of disorder [40], which was not understood before. The electron-phonon scattering time at T_c has also been measured for these films [46], which provides an accurate estimate of τ_0^{scat} and τ_0^{rec} in Eqs. (1) and (3). We analysed those results and find that static scatterers cause a power law temperature dependence of the phonon scattering time with $n = 2$ [36]. Taking this into account, the relaxation times for these TiN films follow both the temperature and disorder dependence of electron-phonon scattering, similar to Fig. 2(a), see Supplementary Section 3. With $r_c \sim \xi^{TiN}$ [1] these films are in the same regime as β -Ta, where $n_{qp}(T) < \tilde{n}_{qp}^{loc}$ and $ql < 1$ (i.e. $\rho_N \gtrsim 10 \mu\Omega\text{cm}$ for a BCS superconductor with $T_c = 1$ K). Therefore, also in these films thermal quasiparticles localize and the recombination process is limited to delocalization via phonon scattering (Fig. 1(d)).

Even in an ordered superconductor a small amount of disorder could induce localized quasiparticle states [1]. In Ref. [35], we observed for Al that there is no effect of phonon trapping on the relaxation time in the saturation regime at low temperatures. We explained that by the presence of an excess number of localized quasiparticles. We estimate that the density of localized quasiparticle states for the quasi-2D Al film is given by, $\tilde{n}_{qp}^{loc} \simeq 1/(\pi r_c^2 d) \approx 160 \mu\text{m}^{-3}$, where we take $r_c \sim \xi^{Al} \approx 200$ nm. If all these states are filled due to a non-equilibrium generation process, the quasiparticle density corresponds to the observed saturation time of 1 ms in Ref. [35]. An increase in disorder increases the number of localized quasiparticle states and decreases this saturation time. This is experimentally shown in [23] for Al and α -Ta. Furthermore, the most disordered Al film in Ref. [23] shows a weaker temperature dependence of τ , which points towards the same phenomenology as observed in Fig. 2(a).

In Fig. 3, we sketch these different quasiparticle recombination regimes. Above the solid line the thermal quasiparticle density is larger than the density of localized quasiparticle states. In that regime, the relaxation time follows the free quasiparticle recombination time, $\tau_{rec}^*(T)$ given by Eqs. (1) and (2) and shown in Fig. 1(c). Below the solid line, quasiparticles localize and recombine within a localization site. The relaxation time saturates to the recombination time at a quasiparticle density equal to the number of localization sites, \tilde{n}_{qp}^{loc} , as observed in Refs. [23, 35]. However, if the phonon scattering time is longer than this saturation time, quasiparticle delocalization via phonon scattering limits

the relaxation and the temperature dependence of the relaxation time is altered to the power-law of τ_{scat} , Eq. (3). This regime is indicated as the light grey area in Fig. 3. The results of Refs. [23, 35, 40], which were previously unexplained, and Fig. 2 are shown in the appropriate disorder and temperature regimes and are consistent with the observed temperature dependence of the measured relaxation times.

A saturation of the quasiparticle relaxation time requires a non-equilibrium quasiparticle generation process such as microwave readout power [19], cosmic rays [16], radioactivity [18] and stray light [17]. In Fig. 3, this can be viewed as a saturation of T/T_c , when T is an effective quasiparticle temperature. We assume that there is a number of excess quasiparticles is present in our experiment due to the continuous microwave read out [19]. The used read out power is equivalent to a number of photons in the resonator of $\bar{n}_{ph} \approx 6 \times 10^4$. If we would minimize this generation process, the quasiparticle relaxation time can become orders of magnitude longer, following the same phonon scattering power law, Eq. (3), down to low temperatures. For example, a relaxation time in granular Al on the order of seconds has been measured at 25 mK with $\bar{n}_{ph} \approx 1 - 300$ and this relaxation time decreases with increasing \bar{n}_{ph} [24].

To conclude, we showed that quasiparticle relaxation in a disordered superconductor (with $ql < 1$) is governed by phonon scattering due to quasiparticle localization (Fig. 1(d)). Because phonon scattering has a weak power-law temperature dependence, disorder results in a short quasiparticle relaxation time at low temperatures. This impacts the performance of superconducting devices. The energy resolving capabilities of Microwave Kinetic Inductance Detectors (MKIDs) [8] are limited by a short quasiparticle relaxation time, which presents a trade-off between photon absorption efficiency (increasing with disorder) and energy resolving power (decreasing with disorder). In quantum circuits, a short relaxation time will help eliminating excess quasiparticles [14], while a steady state number of localized quasiparticles can induce increased microwave loss [24]. Therefore, the fundamentally different quasiparticle dynamics presented in this paper must be considered when implementing disordered superconductors in quantum circuits.

METHODS

Device design and fabrication

The capacitive part of the resonator is an interdigitated capacitor (IDC), with 20 μm wide fingers and 10 μm wide gap. It is patterned using a SF₆ Reactive Ion Etch (RIE) in a 150 nm thick NbTiN film [47] with a critical temperature of 14.0 K and resistivity of 260 $\mu\Omega\text{cm}$. This design

minimizes noise from Two Level Systems (TLS) [48] and ensures that resonance frequency is highly sensitive to changes in the inductive β -Ta section, where the current density is high. The inductor is a strip of β -Ta, see Extended Data Table I, patterned with a SF₆ RIE etch. We place the β -Ta film on a SiN patch, which serves as a membrane for one of the resonators after the Si wafer is etched away from the backside using KOH, see Fig. 2(a) and (b). The inductor is shorted at the end to the NbTiN ground plane to make a quarter wave resonator. Quasiparticles in the β -Ta are confined to the inductor volume due to the higher superconducting gap of the NbTiN. The resonance frequency is 5.1 GHz for the membrane resonator and 5.3 GHz for the substrate resonator, which is set by the finger lengths of the IDC. We set the coupling quality factor, Q_c , to $\sim 10,000$ by tuning the length of the coupling bar next to the read out line. The internal quality factor, Q_i , at 20 mK is approximately 400,000.

Film characterization

To obtain a measure of disorder and electron and phonon dimensionalities, we performed a measurement of the resistance versus temperature, which provides the normal state resistivity, ρ_N , and T_c , the Hall resistance at 1 K, which provides the charge carrier density, n_e , and the upper critical field as a function of temperature, which provides the diffusion constant, D . The results can be found in Extended Data Table I and the details of these measurements are given in Supplementary Section 2. The Ioffe-Regel parameter, $k_F l$, with k_F the Fermi wavenumber and l the electron mean free path, is of order unity. Therefore, the film is electronically disordered and we expect localization effects become important.

For phonon-mediated superconductivity, disorder is characterized with respect to the electron-phonon interaction, i.e. ql , with q the phonon wave number. We calculate ql at two phonon energies: 2Δ , corresponding to recombination phonons and $k_B T$, typical phonon energies for scattering. We use the mass density, $\hat{\rho}$, and the longitudinal and transverse phonon velocities, c_L and c_T , from Ref. [49], see Extended Data Table I. We only consider transverse phonons because these dominate the relaxation rates in our case, as $(c_T/c_L)^3 \ll 1$ [27, 36]. With that, we calculate $q(2\Delta)l = 0.070$ and $q(0.2 \text{ K})l = 0.0046$: both much smaller than 1 so the film is disordered with respect to electron-phonon interactions. We therefore use quasiparticle relaxation time calculations of Reizer and Sergeev [27] and Devereaux and Belitz [28] which are in the disordered limit ($ql \ll 1$), instead of the widely used pure limit ($ql \gg 1$) results of Kaplan et al. [26]. The main difference is that the scattering time (Eq. (3)) has a steeper temperature dependence in the disordered case ($n \rightarrow n + 1$) and the

proportionality constants in Eqs. (1) and (3), τ_{rec}^0 and τ_{scat}^0 , become proportional to $1/\rho_N$, which reflects the weakening of the electron-phonon coupling as disorder increases [42].

For electronic dimensionality, the dirty limit coherence length divided by the film thickness is, $\xi/d = \sqrt{l\xi_0}/d = 0.39 < 1$, with $l = 0.30 \text{ nm}$ and $\xi_0 = 0.79 \mu\text{m}$, the Pippard coherence length. Therefore, the β -Ta film is a 3D superconductor, although it is close to 2D.

For the phonon dimensionality, we compare the phonon wavenumbers to the film thickness, qd . For recombination phonons, the film is 3D ($q(2\Delta)d = 9.3 > 1$) and we can use the results of Ref. [27] for τ_{rec}^0 . For scattering phonons, the film is 2D for $T < 165 \text{ mK}$ (when $q(k_B T)d \leq 1/2$) and 3D for higher temperatures. The phonon dimensionality dictates the temperature dependence, while the electronic dimensionality dictates the disorder dependence [28]. We therefore use the 2D results of Ref. [28] with $n = 7/2$ for the low temperature regime and the 3D result of Ref. [27] with $n = 9/2$ for the high temperatures.

Setup

The sample is cooled in a dilution refrigerator, shielded from stray light with a box-in-a-box setup [17]. Magnetic interference is reduced by a factor 10^{-6} by a CRYOPHY and superconducting niobium shield. The forward transmission measurement is performed in a homodyne setup. The microwave signal is attenuated at each temperature stage before it reaches the sample. After the signal passed the sample, it is amplified by a HEMT amplifier at 3 K and by a room temperature amplifier before it is mixed with the original microwave signal by an IQ mixer. For details on all the components see Ref. [50].

Fluctuation measurement

Before each fluctuation measurement, we sweep the probe frequency to find the resonance frequency, f_0 , and calibrate the complex forward transmission to an amplitude, δA , and phase, θ , with respect to the resonance circle [50]. We set the microwave power of the on-chip probe tone relatively low at -98 dBm to limit non-equilibrium effects such as quasiparticle redistribution [19]. We measure θ during 40 s at 50 kHz sampling frequency and 1 s at 1 MHz. We disregard parts of the time traces that contain pulses from cosmic rays and calculate the Power Spectral Densities (PSDs) [35] and stitch the two PSDs from the 50 kHz and 1 MHz data at 20 kHz to obtain $S_\theta(\omega)$ for a single bath temperature. The fluctuations in

σ_2 , f_0 and θ are related via,

$$\begin{aligned} S_{\delta\sigma_2/|\sigma|}(\omega) &= \left(\frac{4}{\alpha_k\beta}\right)^2 S_{\delta f/f_0}(\omega) \\ &= \left(\frac{1}{\alpha_k\beta Q}\right)^2 S_{\theta}(\omega). \end{aligned} \quad (4)$$

Here, $\sigma = \sigma_1 - i\sigma_2$ the complex conductivity and $|\sigma|$ is the absolute, mean, value at the set bath temperature. At low temperatures ($k_B T \ll \Delta$) $|\sigma| \approx \sigma_2$. $Q = (1/Q_i + 1/Q_c)^{-1}$ is the loaded quality factor and $\alpha_k = L_k/L_{tot}$ is the kinetic inductance fraction of the β -Ta volume with respect to the entire resonator. β is a correction factor for the film thickness, which we set to 2 since we are in the thin film limit ($\lambda \gg d$, with $\lambda \approx 1.6 \mu\text{m}$, the penetration depth) [50].

Q and α_k are measured in a separate measurement where we sweep the probe frequency to get the resonance curve at each bath temperature. We fit a Lorentzian resonance dip to those curves and extract f_0 , Q_i and Q_c versus temperature. From $f_0(T)$ we determine α_k [50], which in our case is $\alpha_k \approx 0.44$.

We disregard the 50 Hz, amplifier and $1/f$ noise contributions in the PSD, see Supplementary Section 4. After that, we fit a Lorentzian spectra to $S_{\delta\sigma_2/|\sigma|}(\omega)$ via,

$$S_{fit}(\omega) = \frac{4s^2\tau}{1 + (\omega\tau)^2}, \quad (5)$$

to extract the variance s^2 and relaxation time τ from the fluctuations.

Data and code availability All presented data and analysis and plotting scripts are available via Zenodo: [10.5281/zenodo.13380277](https://zenodo.org/record/13380277).

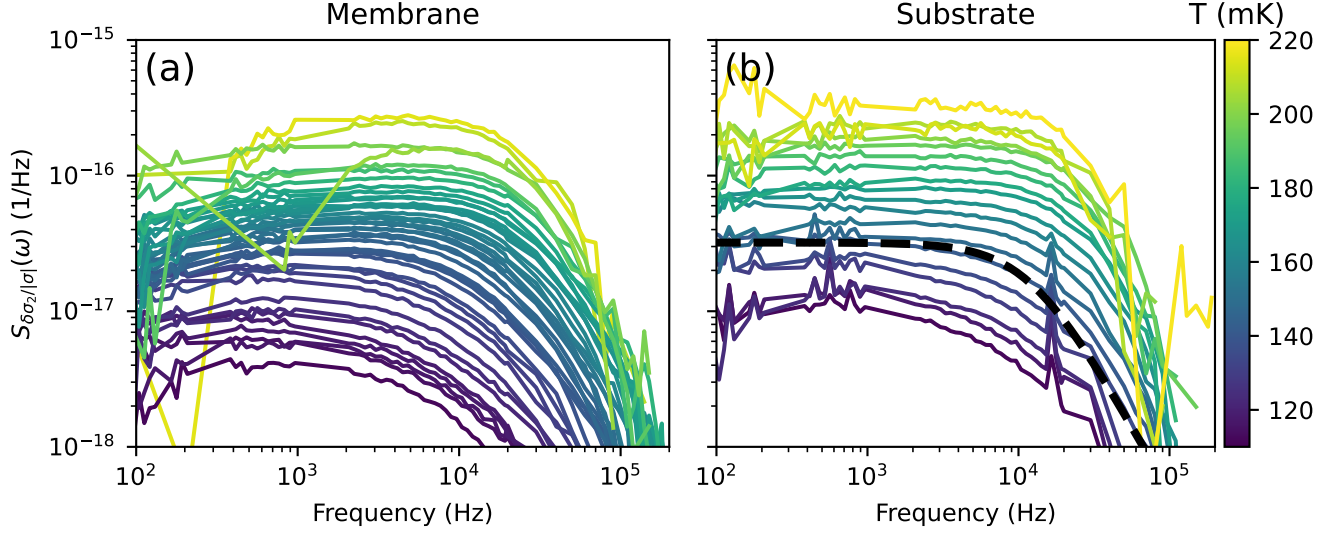
Acknowledgements P.J.d.V. and K.K. were supported by the Netherlands Organisation for Scientific Research NWO (Veni Grant No. 639.041.750 and Projectruimte 680-91-127). J.J.A.B. was supported by the European Research Council ERC (Consolidator Grant No. 648135 MOSAIC).

Author contributions P.J.d.V. and S.A.H.d.R. conceived the experiment. S.A.H.d.R. designed and T.C, V.M. and D.J.T fabricated the device. S.A.H.d.R. performed the microwave measurements, which P.J.d.V. supervised. R.F. performed the characterization measurements, which J.A. supervised. S.A.H.d.R. analysed the data and S.A.H.d.R., R.F., K.K., J.A., J.J.A.B. and P.J.d.V. discussed the results. S.A.H.d.R. wrote the manuscript and R.F., K.K., J.J.A.B. and P.J.d.V. reviewed it substantively. The project was supervised by J.J.A.B. and P.J.d.V.

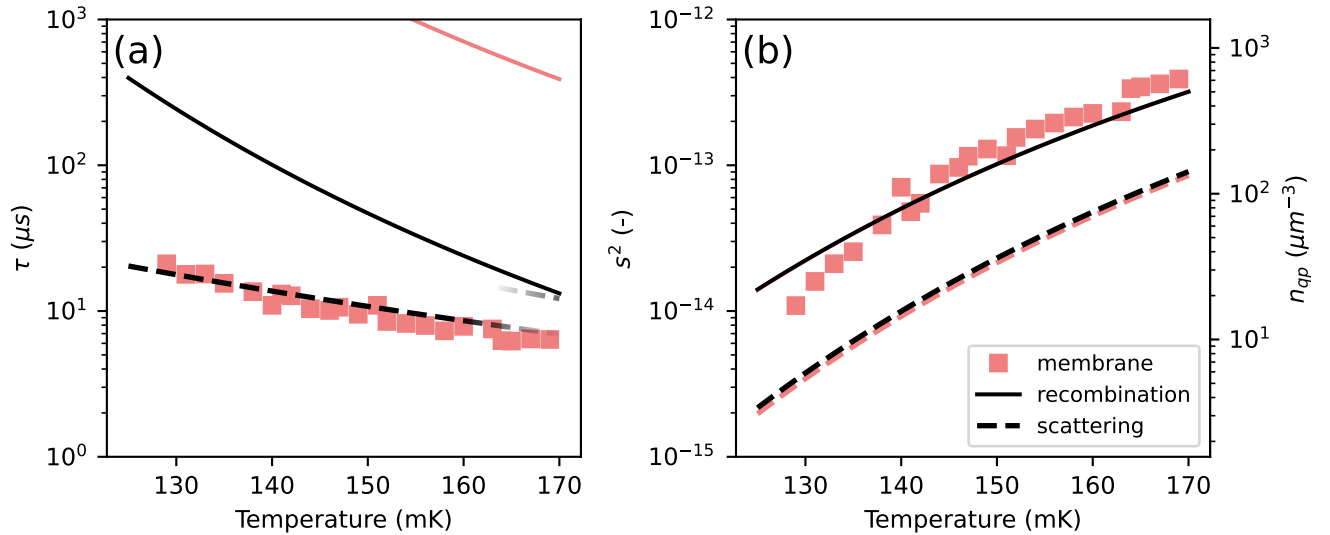
Ethics declarations The authors declare to have no competing interest.

Extended Data Table I. **Geometry, electronic properties and phonon properties for β -Ta.** The electronic properties are obtained via a resistance versus temperature, a Hall resistance versus magnetic field and an upper critical field versus temperature measurement, as set out in Supplementary Section 2.

| Geometry | | | Measured electronic properties | | | | | | Values from Ref. [49] | | | |
|----------|-------------------|-------------------|--------------------------------|---------------------------|----------------------------|------------------------|------|---------|----------------------------|--------|--------|-------|
| d | W | L | T_c | $\rho_N(T = 1 \text{ K})$ | D | n_e | RRR | $k_F l$ | $\hat{\rho}$ | c_L | c_T | T_D |
| (nm) | (μm) | (μm) | (K) | ($\mu\Omega\text{cm}$) | (cm^2/s) | (μm^{-3}) | | | (g/cm^3) | (km/s) | (km/s) | (K) |
| 40 | 10 | 90 | 0.87 | 206 | 0.73 | 1.1×10^{11} | 1.03 | 4.2 | 16.6 | 4.34 | 1.73 | 221 |



Extended Data Fig. 1. **Measured Power Spectral Densities (PSDs) of σ_2 .** Different colors are for different bath temperatures, as indicated by the colorbar. Other noise sources, such as amplifier noise and $1/f$ -noise have been subtracted, as explained in the Supplementary Section 4. The dashed black line in (b) is an example fit using Eq. (5).



Extended Data Fig. 2. **Fluctuation measurement of σ_1 .** Quasiparticle relaxation time (a) and the variance (b) are obtained the same way as in Fig. 2, but from the fluctuations of the dissipative part of the complex conductivity, $\delta\sigma_1$. The quasiparticle signal in σ_1 is a few times lower than in σ_2 [38], which results in a smaller usable temperature range. For the substrate resonator we did not observe any Lorentzian signatures in the PSDs of σ_1 .

Supplementary Information for: 'Recombination of localized quasiparticles in disordered superconductors'

Steven A. H. de Rooij,^{1,2,*} Remko Fermin,^{3,4} Kevin Kouwenhoven,^{1,2} Tonny Coppens,¹ Vignesh Murugesan,¹ David J. Thoen,¹ Jan Aarts,⁴ Jochem J. A. Baselmans,^{1,2} and Pieter J. de Visser¹

¹*SRON - Netherlands Institute for Space Research,
Niels Bohrweg 4, 2333 CA Leiden, The Netherlands*

²*Faculty of Electrical Engineering, Mathematics and Computer Science,
Delft University of Technology, Mekelweg 4, 2628 CD Delft, the Netherlands*

³*Department of Materials Science and Metallurgy, University of Cambridge,
27 Charles Babbage Rd, Cambridge CB3 0FS, United Kingdom*

⁴*Huygens-Kamerlingh Onnes Laboratory, Leiden University, 2300 RA Leiden, The Netherlands*

RELAXATION TIME AND VARIANCE CALCULATIONS

Here we describe how the theory lines in Fig. 2(a) and (b) are calculated. The fluctuation spectrum is given by a Lorentzian, $S(\omega) = 4s^2\tau/(1 + (\omega\tau)^2)$, with τ the relaxation time and s^2 the variance. We will first go over the relaxation time calculations (Fig. 2(a)), including the phonon trapping effect for the β -Ta on substrate and membrane, and then explain how we calculated the variances (Fig. 2(b)).

Relaxation time

Electron-phonon interaction

First, we recall that the β -Ta film is disordered with respect to electron-phonon interactions, i.e. $q(\Omega)l < 1$ with $q(\Omega)$ the phonon wave number and l the electronic mean free path, for both thermal ($\Omega = k_B T$) and recombination ($\Omega = 2\Delta$) phonons. k_B is the Boltzmann constant, T is the bath temperature and 2Δ is the superconducting gap energy.

Second, the film is 2D for $T < 165$ mK thermal phonons ($qd < 1/2$, with d the film thickness) and 3D for higher temperatures and for recombination phonons. We take the values for quasiparticle energy Δ , by which we assume that the quasiparticles are in thermal equilibrium and are all relaxed to the gap energy.

Recombination The 3D case of the recombination time for disordered superconductors is given in Ref. [27], Eq. (61),

$$\tau_{rec}^{e-ph}(T) = \frac{\tau_s(T_c)}{4\pi^{5/2}} \left(\frac{k_B T_c}{2\Delta} \right)^{7/2} \sqrt{\frac{T_c}{T}} e^{\Delta/k_B T}, \quad (\text{S.6})$$

where $\tau_s(T_c)$ is the electron-phonon scattering time in the normal metal at $T = T_c$. This is given in Eq. (31) of Ref. [27] or Eq. (51) of Ref. [36] with $k = 1$:

$$\tau_s(T_c) = \frac{5\hbar^4}{\pi^4} \frac{(k_F c_L)^3}{(k_F l)(k_B T_c)^4 \beta_L \left(1 + \frac{3}{2} \left(\frac{c_L}{c_T} \right)^5 \right)}, \quad (\text{S.7})$$

with,

$$\beta_L = \left(\frac{2E_F}{3} \right)^2 \frac{N_0}{2\hat{\rho}c_L^2}. \quad (\text{S.8})$$

Here, \hbar is the reduced Planck constant, E_F is the Fermi energy, k_F is the Fermi wavenumber, c_L and c_T are the longitudinal and transverse sound velocities, $\hat{\rho}$ is the mass density, T_c is the critical temperature and N_0 is the single spin density of states at the Fermi energy. We use the parameters from Extended Data Table I and calculate N_0 from the Einstein relation, $N_0 = 1/(2e^2\rho_N D)$, with e the electronic charge, ρ_N the normal state resistivity and D the

diffusion constant. For Δ we take the zero temperature BCS value, $\Delta = 1.76k_B T_c$, which is correct up to 0.1%, since we measure at $T < T_c/4$. We assume the free electron model, so we take $k_F = (3\pi^2 n_e)^{1/3}$, where n_e is the charge density, and $E_F = k_F^3 / (4\pi^2 N_0)$. We determine n_e from a Hall resistance measurement and D from an upper critical field measurement, which are explained in the section *Characterization of the β -Ta film*.

Scattering For scattering, we need to distinguish between the 2D and 3D phonon case. The 2D case (for $T > 165$ mK) can be found in Ref. [28], Eq. (4.8a), bottom row:

$$\tau_{scat}^{e-ph, 2D} = \frac{16}{\sqrt{2}} \frac{Z'}{\Gamma(7/2)\zeta(7/2)} \left(\frac{E_F}{\Delta}\right)^2 \frac{c_T \hat{\rho} d}{\Delta k_F^3} \frac{\rho_N e^2}{d\hbar} \frac{c_T^3}{v_F^3} \frac{1}{1 + (c_T/c_L)^4} \left(\frac{\Delta}{k_B T}\right)^{7/2}, \quad (\text{S.9})$$

where Z' is the Eliashberg renormalization constant for the 3D clean limit, $Z' = 1 + N_0 (k_B T_D)^2 v_F^2 / (36 \hat{\rho} c_L^4)$ [51], with T_D the Debye temperature, see Extended Data Table I. v_F is the Fermi velocity, Γ is the gamma function and ζ is the Riemann zeta function.

The 3D case can be found in Ref. [27], Eq. (62),

$$\tau_{scat}^{e-ph, 3D} = \frac{\tau_s(T_c)}{4\pi^2 \Gamma(9/2)\zeta(9/2)} \sqrt{\frac{2\Delta}{k_B T_c}} \left(\frac{T_c}{T}\right)^{9/2}, \quad (\text{S.10})$$

with $\tau_s(T_c)$ given by Eq. (S.7).

Electron-electron interaction

Electron-electron interactions can dominate in disordered metals [52]. However, in a superconductor the normal state charge carrier density is exponentially suppressed, such that the electron-phonon interaction dominates. To quantify that statement, we calculate the electron-electron interactions times here as well.

Our β -Ta film is in the dirty (or impure) regime since, $\xi/l = 62$. l is 0.30 nm and ξ is the dirty limit coherence length, 18 nm. The electron-electron rates in the dirty regime are calculated in Ref. [31], both for 2D and 3D. This is an extension of the theory in Ref. [28] to include gapless collective phase mode in 2D, which occurs when $k_F \xi \lesssim 1$. This collective mode has a power law temperature dependence with $n = 7/2$. In our case, $k_F \xi \approx 262$ so we are not in that regime. Besides that, $\xi/d = 0.47$, so we are not in the 2D but 3D regime. Therefore, the observed power law in Fig. 2 cannot be this gapless phase mode.

All other interaction channels for the electron-electron interaction are gapped and have an exponential temperature dependence. From Ref. [31], Eq. (48), the 3D case, we have,

$$\tau_{rec}^{e-e} = \frac{2^{5/4} (2\pi)^2 \hbar D}{k_B T} \sqrt{\frac{D}{\Delta}} \frac{e^{2\Delta/k_B T}}{(1 + (V_{sc} N_0)^2)}. \quad (\text{S.11})$$

V_{sc} is the BCS attractive potential energy. We calculate this via the BCS gap equation at zero temperature, $1/V_{sc} = N_0 \int_{\Delta}^{k_B T_D} dE / \sqrt{E^2 - \Delta^2} = 1.2 \times 10^5 \mu\text{eV}^{-1} \mu\text{m}^{-3}$.

For scattering, we have from Ref. [31], Eq. (47),

$$\tau_{scat}^{e-e} = \frac{\pi^3 \hbar N_0 D^2}{6\Delta} \sqrt{\frac{D}{k_B T}} e^{4\Delta/5k_B T}. \quad (\text{S.12})$$

In Fig. S3 the recombination and scattering lifetimes for electron-phonon and electron-electron interactions are shown. τ_{rec}^{e-e} is an order of magnitude longer than τ_{rec}^{e-ph} due to the additional factor $e^{\Delta/k_B T}$, which reflects the 3 particle nature of electron-electron recombination instead of 2 quasiparticle electron-phonon recombination.

The electron-electron scattering time is the shortest in this temperature regime. However, this process conserves quasiparticle number and does not change the total energy stored in the quasiparticle system. It only changes the distribution function to the thermal Fermi-Dirac distribution on the time scale of τ_{scat}^{e-e} . As we calculated for electron-phonon scattering, the variance on the kinetic inductance for changes in distribution function are very low (see Fig. 2(b)) and this is not visible in our experiment.

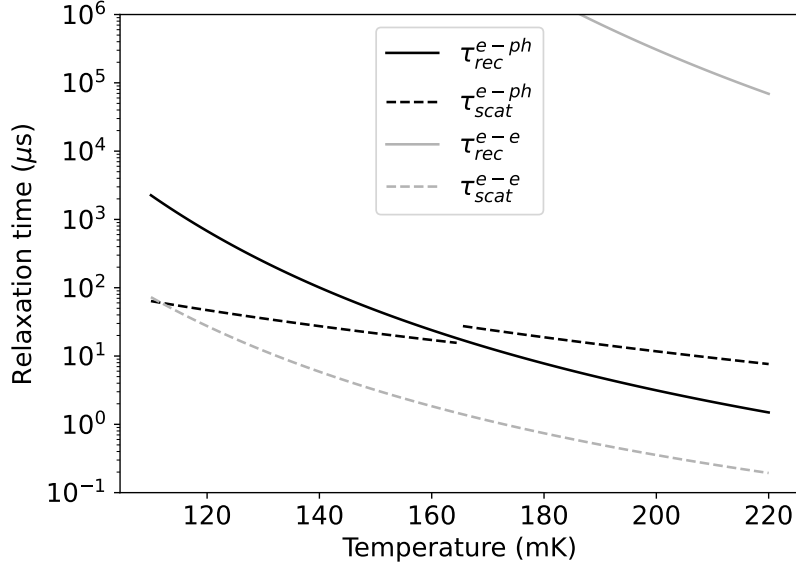


Fig. S3. Electron-phonon and electron-electron relaxation rates from Eqs. (S.6) and (S.9) to (S.12). The temperature range is chosen to match our measurement regime. The electron-phonon times (black solid and dashed lines) are the same as in Fig. 2(a).

Phonon trapping factor

The phonons that are emitted during a recombination event can break other Cooper-pairs, which enhances the measured bulk quasiparticle lifetime. This effect is captured by the phonon trapping factor, $(1 + \tau_{esc}/\tau_{pb})$ in Eq. (2) [30, 32]. We experimentally tune τ_{esc} by measuring the β -Ta on substrate and on a thin membrane. We will first estimate τ_{esc} for β -Ta on a SiN substrate and then estimate the enhanced phonon trapping by the membrane. We assume that phonon scattering on the film boundaries is diffusive. The SiN is etched by a reactive ion etch when patterning the NbTiN before deposition of β -Ta, which makes the interface rough. We only take transverse phonons into account (since $(c_T/c_L)^3 \ll 1$) and neglect phonon loss in the bulk. We then use Eq. (51) of Ref. [34],

$$(1 + \tau_{esc}/\tau_{pb}) = \frac{4d}{\Lambda_T} \frac{1 - (1 - \eta_T)e^{-2d/\Lambda_T}}{\eta_T(1 - e^{-2d/\Lambda_T})}. \quad (\text{S.13})$$

Λ_T is the transverse phonon mean free path against pair breaking, which is given by, $\Lambda_T = c_T\tau_{pb}^T$, with c_T from Table I and τ_{pb}^T the pair breaking time for transverse phonons. We estimate τ_{pb}^T as the inelastic scattering time of phonons in a metal [42, 53],

$$\frac{1}{\tau_{pb}^T} = \frac{n_e m^*}{\hat{\rho}\tau} \left(\frac{1}{\zeta} - 1 \right), \quad (\text{S.14})$$

with $\zeta = 3[(1 + (ql)^2) \tan^{-1} ql - ql]/2(ql)^3$, where $q = 2\Delta/(\hbar c_T)$ is the recombination phonon wave number. n is the charge density, m^* is the effective electron mass, $m^* = 2\hbar^2 N_0 \pi^2 / k_F$ and τ_e is the Drude elastic scattering time, $\tau_e = l/v_F$. This gives $\tau_{pb}^T = 37$ ns, which is relatively long due to disorder, $ql \ll 1$ [42]. Thus, $\Lambda_T = 65$ μm is also large. For example, τ_{pb}^T in Al is 0.12 ns and Λ_T is 0.39 μm .

η_T in Eq. (S.13) is the transmission efficiency for transverse phonons. We calculate it via the acoustic mismatch model from Ref. [33]. The code to calculate the phonon transparencies for an arbitrary interface is available at Zenodo (10.5281/zenodo.13380277).

We use the values from Table I for the β -Ta phonon properties and $\hat{\rho} = 3.1$ g/cm³, $c_T = 6.2$ km/s and $c_L = 10.3$ km/s for SiN [54, 55]. That gives $\eta_T = 0.054$, which results in a phonon trapping factor, from Eq. (S.13), of $(1 + \tau_{esc}/\tau_{pb}) = 2.0$.

To estimate the effect of the membrane, we use a geometrical calculation as shown in Fig. S4. The 2Δ -phonon wavelength is 27 nm, which is smaller but close to $2d = 80$ nm, so a purely geometrical calculation is somewhat

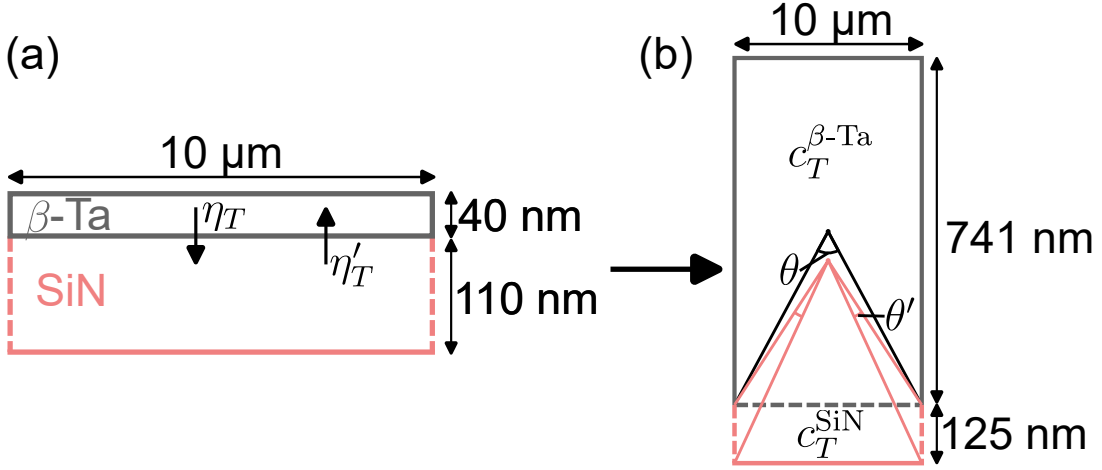


Fig. S4. Illustration of the geometrical calculation to estimate the effect of the membrane on the phonon escape time, τ_{esc} . (a): Situation of the β -Ta film (grey) on the SiN membrane (pink). The physical thicknesses are indicated. The dashed lines indicate that it is not a physical boundary of the material, but only of the volume considered. η_T is the transverse phonon transparency from β -Ta to SiN and η'_T vice versa. (b): Effective film thicknesses d/η_T and d_{SiN}/η'_T , with the phonon escape angles for the substrate case (θ) and the membrane case ($2\theta'$) as indicated.

justified. We will come back to this point at the end of this section.

We calculate the transverse phonon transparency from SiN to β -Ta in the same way as explained above. This results in $\eta'_T = 0.80$. We use the out- and in-going transparencies (η_T and η'_T , respectively) to scale the thickness of the two layers, see Fig. S4(b). With these effective thicknesses, we take the phonon transparencies in the new geometry, Fig. S4(b), to be 1, so we can consider it as one geometrical volume. We assume scattering on the sides is diffusive, such that all the angle dependencies are averaged out. We therefore only consider the escape angles as measured from the centre of the geometrical volume. This is slightly different for the membrane compared to the substrate case, see Fig. S4(b).

For the substrate case we assume a phonon is lost when it enters the SiN. This results in the escape angle θ in Fig. S4(b). For the membrane case, we consider the phonon to be lost when it leaves the volume beneath the β -Ta, which results in an escape angle of $2\theta'$ in Fig. S4(b). The effect of the membrane is given by the ratio of these two escape angles, $\theta/(2\theta')$, when we also compensate for the time that the phonon is in the SiN membrane via the effective thicknesses and transverse sound velocities,

$$\frac{\tau_{esc}^{mem}}{\tau_{esc}^{sub}} = \frac{\theta}{2\theta'} \frac{d/(\eta_T c_T^{\beta-Ta})}{d_{SiN}/(\eta'_T c_T^{SiN}) + d/(\eta_T c_T^{\beta-Ta})} = 60 \times 0.96 = 58. \quad (\text{S.15})$$

This gives a phonon trapping factor of $(1 + \tau_{esc}^{mem}/\tau_{pb}) = 59$. The black line in Fig. 2(c) is given by $\tau_{rec}^* = \tau_{rec}^{e-ph}(1 + \tau_{esc}/\tau_{pb})/2$ (Eq. (2)), where τ_{rec}^{e-ph} is the solid black line in Fig. S3 and $(1 + \tau_{esc}/\tau_{pb}) = 2.0$. The red line in Fig. 2 is the same, but with $(1 + \tau_{esc}/\tau_{pb}) = 59$.

As a check, we perform the exact same calculation for Al on SiN and compare it with Ref. [35]. We come to a phonon trapping factor on SiN substrate of 3.2 and on membrane 17.6. So, a factor 5.5 longer lifetimes are expected. The measurement in Ref. [35] shows an increase in lifetime of a factor 16. Therefore, the assumption of a purely geometric effect of the membrane has limited applicability. For Al, the 2Δ -phonon wavelength is 37 nm, while the film thickness is 50 nm. For higher energetic phonons (i.e. shorter wavelengths) generated by single photon absorption events, such a geometric model is consistent with the data [56]. We therefore expect that the low energetic 2Δ -phonons are trapped more effectively by the membrane than the geometrical calculation predicts. Therefore, we can interpret the above geometric calculation as minimum for the phonon trapping effect of the membrane.

Variance

The theory lines for the variance in Fig. 2(d) are calculated as,

$$s^2 = \langle \delta(\sigma_2/|\sigma|)^2 \rangle = \langle \delta(k_B T)^2 \rangle \left(\frac{d(\sigma_2/|\sigma|)}{dk_B T} \right)^2, \quad (\text{S.16})$$

where the first factor is the variance of the thermal fluctuations and the second is the responsivity to temperature changes. We will calculate these factors for scattering and recombination separately.

Thermal fluctuations

In equilibrium, thermal fluctuations have a variance of $\langle \delta(k_B T)^2 \rangle = k_B^3 T^2 / C$, where $C = dU/dT$ is the heat capacity, with U the internal energy [57].

Recombination For recombination, C is given by the change in quasiparticle number, δN_{qp} , with energy Δ . That gives a heat capacity [58],

$$\begin{aligned} C_{qp} &= \frac{dU}{dT} = \frac{d}{dT} \left(4N_0 V \int_{\Delta}^{\infty} \frac{E^2 f(E; k_B T)}{\sqrt{E^2 - \Delta^2}} dE \right) \\ &\approx \frac{d}{dT} (2N_0 V \Delta^2 [K_0(\Delta/k_B T) + K_2(\Delta/k_B T)]) \\ &\approx \frac{d}{dT} (\Delta N_{qp}) \\ &\approx \frac{N_{qp} \Delta^2}{k_B T^2}. \end{aligned} \quad (\text{S.17})$$

$K_n(x)$ is the n -th modified Bessel function of the second kind. The first approximation is valid for $f(E; k_B T) \approx e^{-E/k_B T}$. The other two are valid for $k_B T \ll \Delta$, which automatically satisfies the first. From this we see that to first order in $k_B T/\Delta$, the internal energy is changed mainly by the change in quasiparticle number and not by the change in distribution function.

If we use this heat capacitance, we come to a variance of

$$\langle \delta(k_B T)^2 \rangle_{rec} = \frac{(k_B T)^4}{N_{qp} \Delta^2}. \quad (\text{S.18})$$

If we multiply this variance with $(dN_{qp}/dk_B T)^2 \approx (N_{qp} \Delta)^2 / (k_B T)^4$, we get N_{qp} , which is the variance of quasiparticle number fluctuations ($\langle \delta N_{qp}^2 \rangle = N_{qp}$). Thus, this is the variance of the temperature fluctuations due to recombination.

Scattering For scattering, we can do something similar as Ref. [38]: we implicitly introduce a chemical potential μ^* to keep N_{qp} constant, while changing $k_B T$. In this case, we need the higher orders in the Bessel functions $K_0(\Delta/k_B T)$ and $K_2(\Delta/k_B T)$, to get the first order in explicit temperature dependence of U . So,

$$\begin{aligned} U &= N_0 V \Delta \sqrt{2\pi k_B T \Delta} e^{-\frac{\Delta}{k_B T}} \left(1 + \frac{k_B T}{\Delta} \right) \\ &= \Delta N_{qp} \left(1 + \frac{k_B T}{\Delta} \right). \end{aligned} \quad (\text{S.19})$$

Now,

$$C_{rec} = \frac{\partial U}{\partial N_{qp}} \frac{dN_{qp}}{dT} = \frac{N_{qp} \Delta^2}{k_B T^2}, \quad (\text{S.20})$$

and

$$C_{scat} = \frac{\partial U}{\partial T} = k_B N_{qp}. \quad (\text{S.21})$$

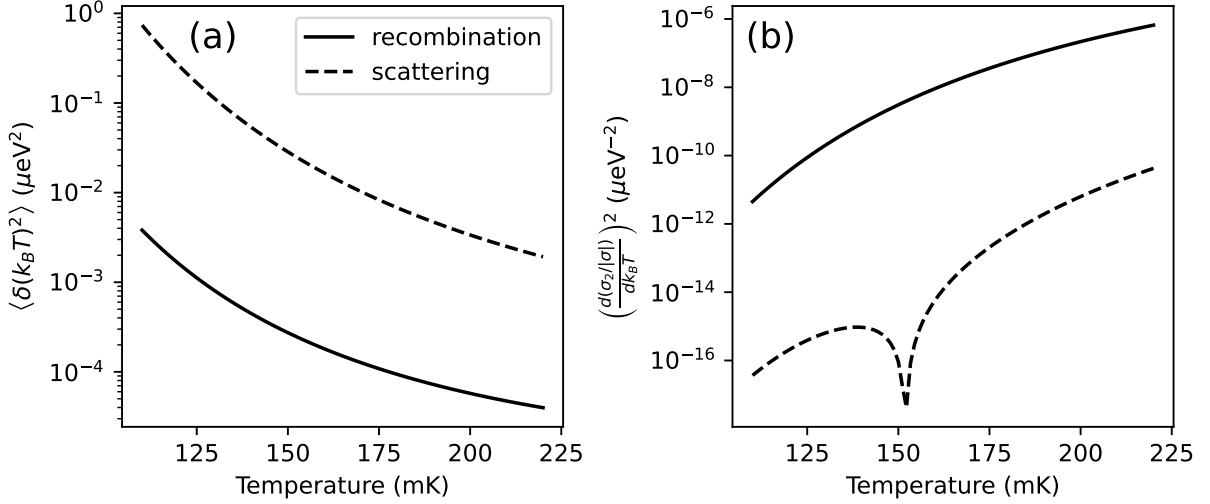


Fig. S5. Contributions to the variance calculations. (a): Thermal fluctuation variance for recombination, Eq. (S.18), and scattering, Eq. (S.23). (b): Temperature responsivity of $\sigma_2/|\sigma|$ from Eq. (S.26). The legend is applicable to (a) and (b). For the calculations we set $\omega_0/2\pi = 5$ GHz and use the properties of β -Ta from Table I. The multiplication of the curves in (a) and (b) give the theory lines in Fig. 2(b).

The total variance can be written,

$$\langle \delta(k_B T)^2 \rangle = \frac{k_B^3 T^2}{C_{rec} + C_{scat}} \approx \frac{(k_B T)^4}{N_{qp} \Delta^2} \left[1 - \left(\frac{k_B T}{\Delta} \right)^2 \right], \quad (\text{S.22})$$

where the approximation is valid for $k_B T \ll \Delta$. This shows that scattering only gives a small negative correction to the variance of the temperature fluctuations. It is a negative correction, as the change in $k_B T$ enhances the heat capacity.

If the number of quasiparticles stays constant, $C_{rec} = 0$ and we would be left with,

$$\langle \delta(k_B T)^2 \rangle_{scat} = \frac{k_B^3 T^2}{C_{scat}} = \frac{(k_B T)^2}{N_{qp}}. \quad (\text{S.23})$$

This is larger than $\langle \delta(k_B T)^2 \rangle_{rec}$ by a factor $(\Delta/k_B T)^2$, which is $\sim 10^2$ in our measurement, see Fig. S5(a). We use Eq. (S.23) for the variance of scattering events. It is however only valid when the number of quasiparticles stays constant. This is true when $\tau_{scat} \ll \tau_{rec}$, which is valid for $T \lesssim 130$ mK in our case, see Fig. S3. When this condition is not satisfied, the variance will be dominated by recombination events. Therefore, Eq. (S.23) can be viewed as an upper limit for the complete measurement range.

Responsivities

The second factor in Eq. (S.16) is the temperature responsivity of $\sigma_2/|\sigma|$ squared. We calculate this factor for recombination and scattering separately. We use the methods of Ref. [38] to calculate these responsivities from the Mattis-Bardeen equations [37]. For completeness, we show the calculations for both σ_1 and σ_2 .

For recombination, we assume that the temperature is constant, while the number of quasiparticle changes with the use of a chemical potential. We can use Eqs. (18) and (19) from Ref. [38] and multiply by

$$\frac{dn_{qp}}{dk_B T} \approx \frac{n_{qp} \Delta}{(k_B T)^2}. \quad (\text{S.24})$$

The approximation is valid for low temperatures, $k_B T \ll \Delta$. This results in,

$$\begin{aligned} \left. \frac{d\sigma_1}{dk_B T} \right|_{rec} &= \frac{\sigma_n n_{qp}}{N_0 \hbar \omega} \sqrt{\frac{2\Delta^3}{\pi(k_B T)^5}} [\sinh(\chi) K_0(\chi)] \\ \left. \frac{d\sigma_2}{dk_B T} \right|_{rec} &= -\frac{\sigma_n n_{qp}}{N_0 \hbar \omega} \sqrt{\frac{\pi\Delta^3}{2(k_B T)^5}} \left[\sqrt{\frac{\pi k_B T}{2\Delta}} + e^{-\chi} I_0(\chi) \right], \end{aligned} \quad (\text{S.25})$$

with, $\chi = \hbar\omega_0/2k_B T$. $I_0(\chi)$ is the zero-order modified Bessels function of the first kind. ω_0 is the angular resonance frequency of the resonator.

For scattering, we assume that the number of quasiparticles is constant, but $k_B T$ changes. We take Eqs. (16) and (17) from Ref. [38] and differentiate with respect to $k_B T$ to find:

$$\begin{aligned} \left. \frac{d\sigma_1}{dk_B T} \right|_{scat} &= \frac{\sigma_n n_{qp}}{N_0 \hbar \omega} \sqrt{\frac{\Delta}{2\pi(k_B T)^3}} [2\chi (\sinh(\chi) K_1(\chi) - \cosh(\chi) K_0(\chi)) - \sinh(\chi) K_0(\chi)] \\ \left. \frac{d\sigma_2}{dk_B T} \right|_{scat} &= \frac{\sigma_n n_{qp}}{N_0 \hbar \omega} \sqrt{\frac{\pi\Delta}{8(k_B T)^3}} [e^{-\chi} (I_0(\chi) + 2\chi (I_1(\chi) - I_0(\chi)))]. \end{aligned} \quad (\text{S.26})$$

We divide Eqs. (S.25) and (S.26) by $|\sigma(T)| = |\sigma_1 - i\sigma_2|$, which we calculate $\sigma(T)$ from the Mattis-Bardeen equations [37]. When we square the result, we get for $\sigma_2/|\sigma|$ the values plotted in Fig. S5(b), for $\omega_0/2\pi = 5$ GHz and the material parameters for β -Ta from Table I.

The responsivity for scattering events is ~ 5 orders of magnitude lower than for recombination. This can also be seen from the curves in Fig. 1 of Ref. [38]: to first order, the scattering responsivity of σ_1 and σ_2 is equal to the difference of the thermal and excess quasiparticle responsivity curves. This is very small, but grows for higher temperatures.

The dip around 150 mK in Fig. S5(b) is at the point where $\chi \approx 0.79$, or $k_B T \approx 0.63\hbar\omega_0$. At that value of χ , the term in square brackets in the lower equations of Eq. (S.26) vanishes.

The curves in Fig. 2(b) are the multiplication of the curves in Fig. S5(a) and (b), but with the actual resonance frequencies. The variance of thermal fluctuations is ~ 2 order of magnitude higher but the responsivity is ~ 5 orders of magnitude lower. Therefore, the variance of σ_2 -fluctuations is ~ 3 orders of magnitude lower for scattering events, which is shown in Fig. 2(b).

As the substrate and membrane resonator have a slightly different resonance frequency the dip in Fig. S5(b) is at a different location. That results in the difference for the variance of σ_2 -fluctuations for scattering events in Fig. 2(b).

CHARACTERIZATION OF THE β -Ta FILM

We characterize the β -Ta film in three ways: (1) a resistance versus temperature measurement; (2) a Hall resistance versus magnetic field and (3) a upper critical field measurement versus temperature. The first is measured in the same setup as the measurements presented in the main text, but at a different, thermally weakly coupled, stage. The resistance measurements are done with a Lakeshore model 372 AC resistance bridge.

The Hall resistance and upper critical field measurement are performed in a different setup, which includes a superconducting coil to apply a magnetic field up to 6 T, which is orientated in the out-of-plane direction with respect to the β -Ta film. In this setup, the resistance measurements are performed with a SynkTek MCL1-540 lock-in amplifier. The 4-probe and Hall bar structures used for these measurements are fabricated on the same wafer as the devices presented in the main text. The geometries are shown in the insets of Fig. S6.

Resistance versus temperature

The resistance measurement is shown in Fig. S6(a). From this measurement, we get a critical temperature of $T_c = 0.87$ K shown by the dashed line. We choose T_c as the temperature where the resistance is approximately half the normal state resistance. We measure the normal state resistance to be $R_N = 661 \Omega$ at 1.0 K, which equals a normal state resistivity $\rho_N = 206 \mu\Omega\text{cm}$ when taking the geometry in Fig. S6(a) into account.

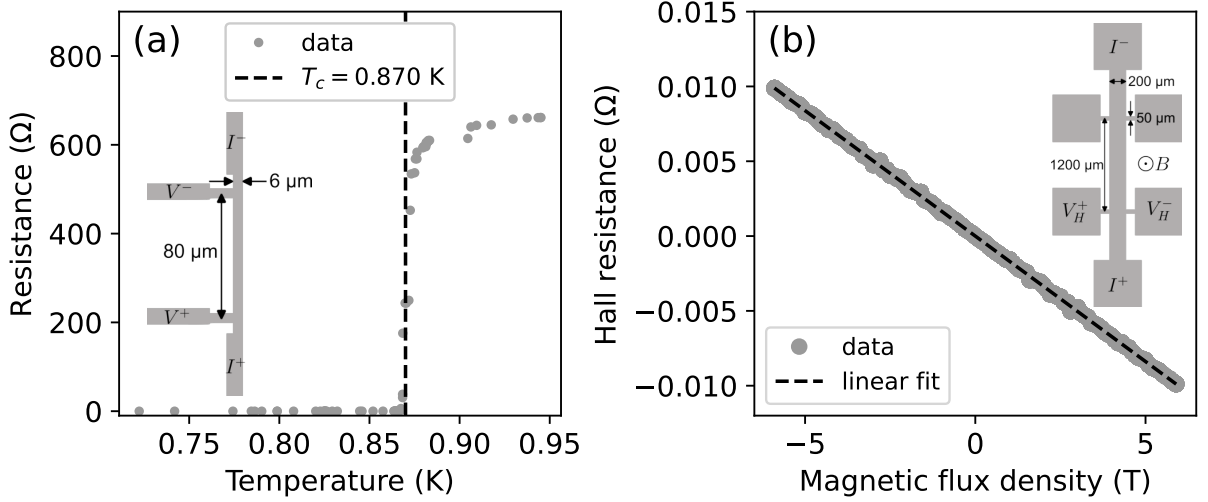


Fig. S6. Transport measurements characterizing the β -Ta film. (a): Resistance measurement versus temperature in the absence of magnetic field. The dashed line give the critical temperature we use in the analysis. The inset shows the geometry which is used for the measurement. (b): Anti-symmetrized Hall resistance (V_H/I) measurement, performed at 1 K. The standard deviation for each data point is smaller than the marker size. The dashed line gives a linear fit with a slope of $dR_H/dB = 1.68 \times 10^{-3} \Omega/T$. The inset shows the Hall bar geometry and contacts used for the measurement. The measurement in (a) is performed with a different setup than the measurement in (b). The devices are from the same wafer as the devices shown in Fig. 2(a).

Hall resistance

The Hall resistance measurement is performed at 1.0 K bath temperature and with the geometry shown in the inset of Fig. S6(b). The dashed line shows a linear fit to the data, with $dR_H/dB = 1.68 \times 10^{-3} \Omega/T$. The raw resistance measurement data is anti-symmetrized with respect to the magnetic field ($R_{Hall} = (R_T(B) - R_T(-B))/2$) to eliminate of any longitudinal resistance component. From the fitted slope we can find the charge carrier density,

$$n_e = \frac{1}{ed} \left(\frac{dR_{Hall}}{dB} \right)^{-1} = 9.3 \times 10^{28} \text{ m}^{-3}, \quad (\text{S.27})$$

where e is the electron charge and d is the film thickness. Assuming the free electron model to hold, we can calculate the Fermi wavenumber as, $k_F = (3\pi^2 n_e)^{1/3} = 14 \text{ nm}^{-1}$. The Ioffe-Regel parameter is given by, $k_F l = \hbar(3\pi^2)^{2/3}/(n_e^{1/3} e^2 \rho_N) = 4.2$. This also gives the electron mean free path, $l = 0.30 \text{ nm}$.

Upper critical field

The only other parameter missing for the calculations of the scattering times and variance is the single spin density of states at the Fermi level, N_0 . We use the Einstein relation, $N_0 = 1/(2e^2 \rho_N D)$ to calculate N_0 from the diffusion constant D . This can be measured in superconductors from the temperature dependence of the upper critical field, $H_{c2}(T)$. Specifically [59, 60],

$$D = \frac{4k_B}{\pi e} \left(\left. \frac{d(\mu_0 H_{c2})}{dT} \right|_{T=T_{c0}} \right)^{-1}. \quad (\text{S.28})$$

T_{c0} is the critical temperature at zero field. To determine the slope of $B_{c2}(T) = \mu_0 H_{c2}(T)$ at T_{c0} , we measure resistance versus temperature curves for different applied fields, as shown in Fig. S7(a). We use the same Hall bar geometry as shown in the inset of Fig. S6(b) to measure the longitudinal resistance. We determine the critical temperature for a given magnetic field as the temperature where the resistance is 50% of the normal state resistance, and invert that to get $B_{c2}(T)$. The result is shown in Fig. S7(b).

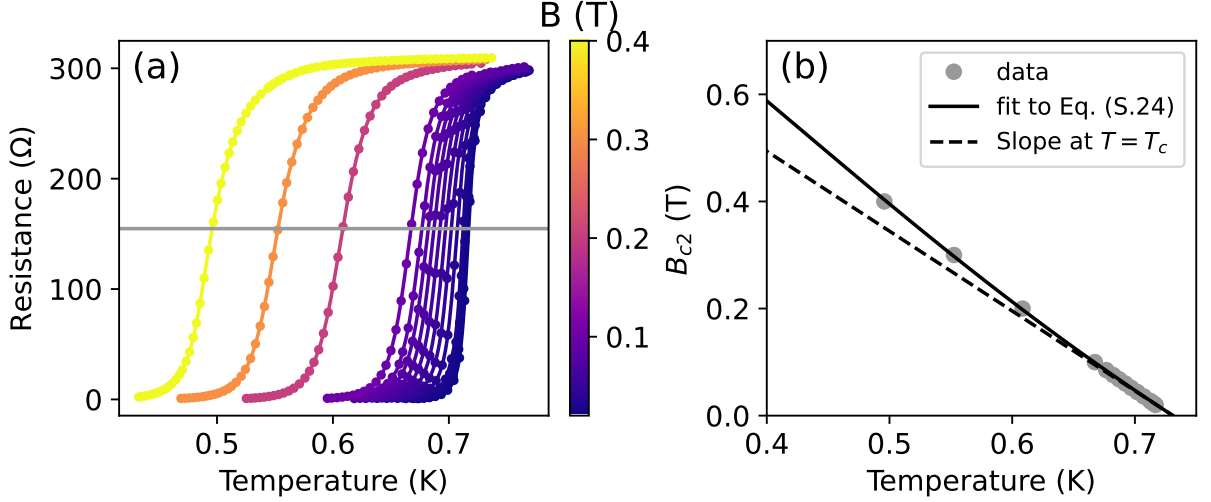


Fig. S7. Upper critical field measurement versus temperature. (a): Resistance versus temperature at different magnetic flux densities, see the colour bar. The dots are data points and the solid lines are cubic spline fits for each value of B . The grey line indicates where we chose to define B_{c2} , which is arbitrary for our analysis as long as it is in the transition. The measured device is depicted in the inset of Fig. S6(b), where we measure the resistance over two lateral contacts. (b): The grey dots are the extracted upper critical field from the intersection of the grey line and the individual spline fits in (a). The black solid line is a fit to Eq. (S.29), with $B_{c2}(0)$ and T_{c0} as free parameters. The dashed line gives the slope at T_{c0} , $dB_{c2}/dT|_{T=T_{c0}} = -2.0$ T/K.

To account for a slight non-linearity of $B_{c2}(T)$ at T_{c0} , we fit $B_{c2}(T)$ to the function [61],

$$B_{c2}(T) = B_{c2}(0) \left(\frac{1 - (T/T_{c0})^2}{1 + (T/T_{c0})^2} \right), \quad (\text{S.29})$$

where $B_{c2}(0)$ is the upper critical flux density at $T = 0$. We use both $B_{c2}(0)$ and T_{c0} as fit parameters and we are interested in ratio, which gives the slope of $B_{c2}(T)$ at T_{c0} . The fit is shown in Fig. S7(b) as the solid black line together with the slope at T_{c0} as dashed line, which is $dB_{c2}/dT|_{T=T_{c0}} = -1.5$ T/K.

This slope gives from Eq. (S.28) $D = 0.74$ cm^2/s , and $N_0 = 2.1 \times 10^4$ $\mu\text{eV}^{-1}\mu\text{m}^{-3}$, which is comparable to the value 3.1×10^4 $\mu\text{eV}^{-1}\mu\text{m}^{-3}$ from Ref. [62]. These values result in a Ginzburg-Landau coherence length of $\xi_{GL} = 16$ nm.

Surprisingly, we find from Fig. S7(b) $T_{c0} = 0.72$ K, while we found $T_c = 0.87$ K in Fig. S6(a). We verified this lower T_c for the Hall bar structure in the setup without magnetic field which was used to obtain the data in the main

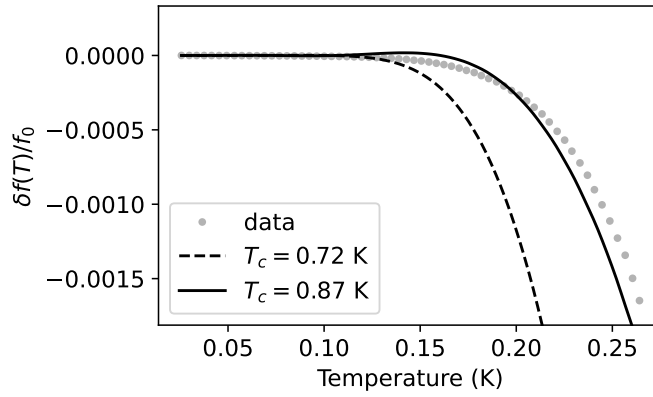


Fig. S8. Fractional frequency shift with temperature of the membrane resonator compared to Mattis-Bardeen theory [37] to verify the critical temperature of $T_c = 0.87$ K. The dashed and solid lines are calculated with the parameters in Table I, $\alpha_k^{sim} = 0.66$ from simulation and T_c as indicated by the legend.

text. The 4-probe and Hall bar structures are patterned in the same deposited film and close together on the wafer. The main difference is the width of the structures: 6 μm versus 200 μm , see the insets of Fig. S7(a) and (b). Why this would change the T_c is not known, although it could be related to the stress in the film that might change the electron-phonon coupling for different widths. Nonetheless, we use the Hall bar geometry to extract normal state electronic properties only, namely the diffusion constant and the carrier charge density. For the diffusion constant, $D \propto T_c/B_{c2}$ with, in the dirty limit, $B_{c2} \propto 1/\xi_{GL}^2 \propto 1/\xi_0 \propto T_c$, where ξ_0 the BCS coherence length. From this, we see that the diffusion constant does not depend on T_c to first order. The carrier charge density is extracted in the normal state. Therefore, we expect that the different T_c of the Hall bar does not have an effect on the extracted properties.

We take $T_c = 0.87$ K for the inductors, as they are 10 μm wide, which similar to the 4-probe structure width. We verify this T_c by comparing the measured fractional resonance frequency shift versus temperature, $\delta f(T)/f_0$, to the calculated curves from Mattis-Bardeen [37] with $T_c = 0.72$ K and $T_c = 0.87$ K as input. We used a kinetic induction fraction of $\alpha_k^{sim} = 0.66$ from a simulation, since the measurement of $\alpha_k = 0.44$ assumes that $T_c = 0.87$ K. This comparison is shown in Fig. S8, from which, we conclude that the inductors have a T_c of 0.87 K. The small deviations from the solid line are most likely due to the disorder in the film, as disordered superconductors behave slightly differently than predicted by standard Mattis-Bardeen theory [63, 64].

TiN DATA ANALYSIS

The electron-phonon scattering time has a weak power-law temperature dependence (Eq. (3)), which contrasts the exponential temperature dependence of conventional quasiparticle recombination (Eq. (1)). This weak temperature dependence has also been measured with TiN resonators in Ref. [40]. There, the relaxation time is measured as the decay time of a pulsed excitation, which is either generated by a (high photon number) LED pulse, or a microwave pulse applied to the read-out line of the resonators. The normal state electron-phonon times of these 3 films have been measured in Ref. [46], where they suppress T_c using a magnetic field. The results of these measurements are shown in Fig. S9. In this section, we analyse the three films from Ref. [40], C, D and E, in the same manner as we analysed the β -Ta film in the main text.

The parameters used for the calculations are shown in Table S2. The first 6 columns are from Refs. [40, 46] and give us the electronic properties. From the k_{Fl} values we see that these films are indeed disordered, but somewhat less than the β -Ta film from the main text. To estimate the rest of the electronic properties, we need N_0 as well. This has been measured in Ref. [65] for similar films. We compare the thickness of each film and estimate N_0 to be the values in Table S2. With these values, we calculate $\xi/d \lesssim 0.25$. So, these are 3D superconducting films.

We estimate the phonon properties of the TiN films in the following way. The mass density we get from Ref. [66], for TiN film with similar thickness. The Debye temperature we get from Ref. [67]. The transverse and longitudinal sound velocities, we estimate from a fit to the data for Ref. [46]. This is procedure is also set out in Ref. [68]. We assume $c_T = c_L/2$ and let c_L be a free fit parameter. This relation seems to be correct for many materials [26]. The results do not change if we assume $c_T < c_L/2$, since the relaxation times are then limited by transverse phonon scattering and we are left with only one sound velocity. To fit the measured electron-phonon relaxation times, we use the theory of Ref. [36], which includes static scatterers when $k \leq 1$. We use Eq. (51) of [36],

$$\begin{aligned} \frac{1}{\tau_s(T)} = & \frac{\pi^4 \beta_L (k_{Fl})(k_B T)^4}{5\hbar^4 (k_F c_L)^3} \left(1 + k \frac{3}{2} \left(\frac{c_L}{c_T} \right)^5 \right) \\ & + \frac{3\pi^3 \beta_L (k_B T)^2}{2\hbar^2 (k_{Fl})(k_F c_L)} (1 - k) \left(1 + 2k \left(\frac{c_L}{c_T} \right)^3 \right). \end{aligned} \quad (\text{S.30})$$

β_L is defined in Eq. (S.8). These measurements are performed at a finite temperature, above T_c , where the electrons distributed in energy around the Fermi surface with a width of $k_B T$. The measured signal is an average of all these electrons. So, the measured $\tau_s^{\text{meas.}}$, is given by [68, 69],

$$\frac{1}{\tau_s^{\text{meas.}}(T)} = \frac{3(n+2)\Gamma(n+2)\zeta(n+2)}{2\pi^2(2-2^{1-n})\Gamma(n)\zeta(n)} \frac{1}{\tau_s(T)}. \quad (\text{S.31})$$

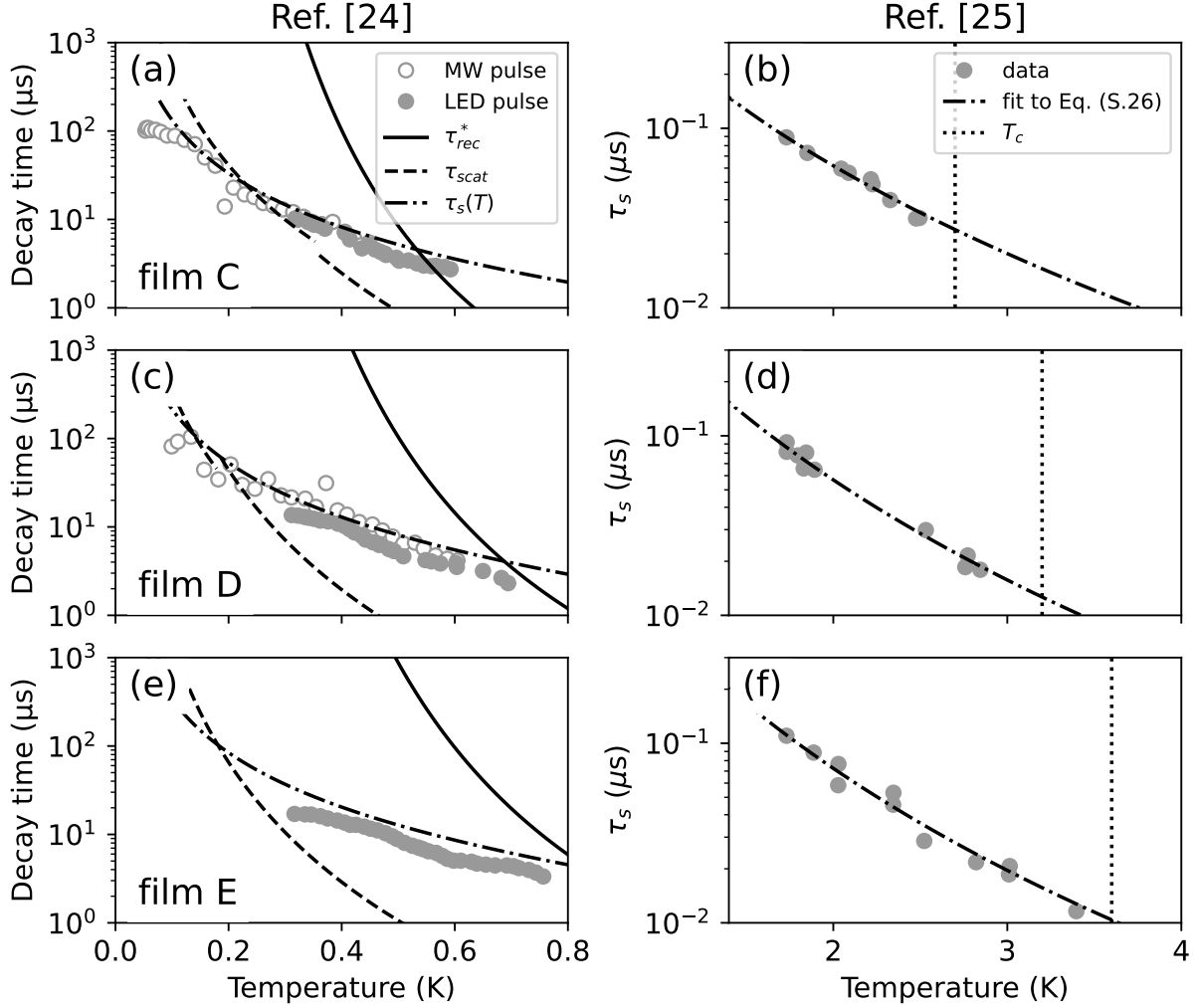


Fig. S9. Relaxation times of three different TiN films from Refs. [40, 46], compared to disorder theory of Refs. [27, 28, 36]. (a), (c) and (e): Decay times of a pulse response from Ref. [40]. Solid grey dots are for a LED pulse and the open grey circles are for a microwave pulse applied at the resonator read-out line. The solid line is given by Eq. (2), with τ_{rec} given by Eq. (S.6) and the phonon trapping factor given by Eq. (S.13). The dashed lines are from Eq. (S.9) for low temperatures ($T < \hbar c_T / (2dk_B)$) and from Eq. (S.10) for high temperatures ($T > \hbar c_T / (2dk_B)$). (b), (d) and (f): The electron-phonon scattering time as measured in [46], for the same films as (a), (c) and (e), respectively. The dotted vertical line indicates the critical temperature. The dashed-dotted black line is a fit to Eq. (S.31), with k and c_L as free parameters and assuming $c_T = c_L/2$. The dashed-dotted lines in (a), (b) and (c) is the same, but without correction factor from Eq. (S.31). The legends are applicable to all the figures in the same column. We used the parameters from Table S2 to calculate the theoretical lines.

For n we use the values from [46], see Table S2. We use Eq. (S.31) to fit the the data of [46], as shown in Fig. S9(b), (d) and (f). The fit results are given in the two right columns of Table S2.

With also the sound velocities available, we can estimate the phonon dimensionality via qd and disorder via ql . For thermal phonons, we find that $q(k_B T)d = 1/2$ at 0.36 K, 0.18 K and 0.11 K, for film C, D and E respectively. Below these temperatures, the thermal phonons are 2D, above them they are 3D. Recombination phonons are 3D, $q(2\Delta)d \geq 13$ for all films.

Electron phonon interaction is disordered, since both $q(2\Delta)l \leq 0.46$ and $q(0.8 \text{ K})l \leq 0.03$ are smaller than one. We therefore use the same equations as for β -Ta, namely Eq. (S.6) for recombination and Eqs. (S.9) and (S.10) for scattering.

We calculate the phonon trapping factor in the same manner as for β -Ta, i.e. Eq. (S.13), but with the parameters in Table S2. The substrate is in this case Si, for which we use: $\hat{\rho} = 2.33 \text{ g/cm}^3$, $c_L = 8.98 \text{ km/s}$ and

Table S2. Parameters for the TiN films from Refs. [40, 46], with additional parameters estimated from Refs. [65–67]. N_0 and $\hat{\rho}$ are estimated from similar films taking the thickness into account. n is the power of the temperature dependence of τ_s , as measured in [46]. c_L and k are the results of the fits in Fig. S9(b), (d) and (f), using Eq. (S.31) and assuming $c_T = c_L/2$.

| Film | From Refs. [40, 46] | | | | | Ref. [65] | Ref. [66] | Ref. [67] | Fit Ref. [46] to Eq. (S.31) | |
|------|---------------------|-----------|-----------------------------------|----------|-----|---|---|-----------|-----------------------------|-------|
| | d (nm) | T_c (K) | ρ_N ($\mu\Omega\text{cm}$) | k_{Fl} | n | N_0 ($\mu\text{eV}^{-1}\mu\text{m}^{-3}$) | $\hat{\rho}$ (g/cm^3) | T_D (K) | c_L (km/s) | k |
| C | 22 | 2.7 | 253 | 4.6 | 2.8 | 6.2×10^4 | 5.7 | 579 | 4.0 | 0.993 |
| D | 45 | 3.2 | 187 | 6.1 | 3.1 | 6.0×10^4 | 5.0 | 579 | 4.2 | 0.995 |
| E | 89 | 3.6 | 120 | 8.6 | 3.3 | 5.9×10^4 | 5.0 | 579 | 5.1 | 0.995 |

$c_T = 5.34$ km/s [33]. The diffuse scattering assumption is in this case justified by the presence of a native oxide layer between the TiN and the Si. Furthermore, the TiN films are polycrystalline with a grain size smaller than 42 nm [40]. We get from Eq. (S.13) a phonon trapping factor of 29, 96 and 193 for films C, D and E, respectively. As an example, for film D the pair breaking time is on the order of 2 ns and phonon escape time on the order of 200 ns.

The resulting scattering and recombination times are shown in Fig. S9(a), (c) and (e) by the dashed and solid lines. The measured quasiparticle relaxation times have an even weaker temperature dependence than the phonon scattering time, $n < 9/2$. However, the theory of Refs. [27, 28] do not take static scattering into account, while we see from the fit results in Table S2 that $k < 1$ for all films. A theory for inelastic electron-phonon scattering in superconductors that includes static scatterers is still lacking. Nonetheless, we can compare the quasiparticle relaxation times to the normal state scattering time, $\tau_s(T)$. From Eq. (S.30) we see that static scatterers cause a $n = 2$ power-law when $k < 1 - (k_B T l / (\hbar c_T))^2 < 0.999$ [36], which is satisfied in all experimental regimes in Fig. S9(a), (c) and (e). We plotted $\tau_s(T)$ from Eq. (S.30) with the same film parameters and no fit parameter. We omitted the averaging factor in Eq. (S.31), as the quasiparticles in a superconductor all have an energy very close to Δ due to the gap in the density of states.

We observe that the relaxation times follow the same $n = 2$ temperature dependence for all film. The disorder dependence of the relaxation rate is also captured by Eq. (S.30), since the difference between the data and Eq. (S.30) is constant for the variation in disorder in the different films. We therefore conclude that also in TiN, the quasiparticle relaxation is enhanced and governed by the phonon scattering time. It also shows that this phenomenology is not limited to the β -Ta film we study in the main text, but is present in different disordered superconductors.

If we take $\xi^{TiN} \approx 6$ nm as localization length, we get a density of localized quasiparticle states of $n_{qp}^{loc} = 3/(4\pi(\xi^{TiN})^3) \approx 1 \times 10^6 \mu\text{m}^{-3}$. The thermal quasiparticle density at the maximum measured temperatures in Fig. S9(a), (c) and (e) is $n_{qp}^T \approx 7 \times 10^3 \mu\text{m}^{-3}$. This shows we are in the same regime as the β -Ta film of the main text: the thermally excited quasiparticles localize and recombine after delocalization by electron-phonon scattering. The values mentioned are based on the parameters in Table S2 and are the same within a factor 2 for all three films.

FITTING THE POWER SPECTRAL DENSITIES

The measured raw power spectral density (PSD) is shown in Fig. S10(a) as the dark blue line. This example is at the low temperature end of our measurement regime, 135 mK, where the contribution from other noise sources is significant. Contributions from 50 Hz interference, $1/f$ fluctuators and the 4 K HEMT amplifier are clearly visible in the PSD. To minimize the effects from these noise sources to the Lorentzian fit, we first disregard the data points in the grey shaded regions in Fig. S10(a). Second, we take the maximum value between 250 kHz and 500 kHz as the amplifier noise contribution and subtract that from the PSD. The value is shown by the grey dashed line. Third, we fit the function, A/f^γ , from 3 Hz to 100 Hz with A and γ as fit parameters. The fit is shown as the grey solid line, which is also subtracted from the PSD. The resulting PSD is shown in Fig. S10(b) as the dark blue line. We fit Eq. (5) to this PSD, which results in the black dashed line and gives us τ and s^2 in Fig. 2(c) and (d).

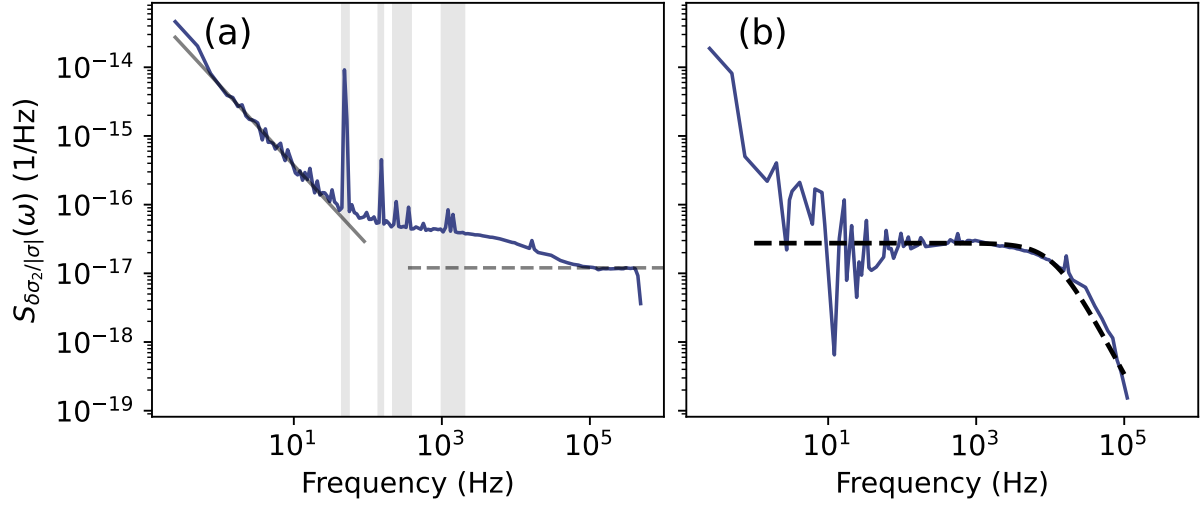


Fig. S10. Example of the subtraction of other noise sources and fitting of the measured kinetic inductance fluctuation power spectral density (PSD). (a): Measured raw PSD in dark blue for the substrate resonator at 135 mK. The grey shaded vertical areas indicate the frequency ranges that we disregard to limit the influence of 50 Hz spikes. The dashed line grey gives the maximum of the data between 250 kHz and 500 kHz, which we subtract as amplifier noise. The solid grey line gives a A/f^γ -fit, with A and γ as fit parameters. We subtract the result of the fit to limit the effects of $1/f$ noise. (b): Resulting power spectral density in dark blue with the Lorentzian fit, Eq. (5), as black dashed line.

* s.a.h.de.rooij@sron.nl

- [1] A. Beshpalov, M. Houzet, J. S. Meyer, and Y. V. Nazarov, Theoretical Model to Explain Excess of Quasiparticles in Superconductors, *Physical Review Letters* **117**, 117002 (2016).
- [2] M. V. Feigel'man and M. A. Skvortsov, Universal Broadening of the Bardeen-Cooper-Schrieffer Coherence Peak of Disordered Superconducting Films, *Physical Review Letters* **109**, 147002 (2012).
- [3] A. I. Larkin and Y. N. Ovchinnikov, Density of States in Inhomogeneous Superconductors, *Soviet Journal of Experimental and Theoretical Physics* **34**, 1144 (1972).
- [4] B. Sacépé, M. Feigel'man, and T. M. Klapwijk, Quantum breakdown of superconductivity in low-dimensional materials, *Nature Physics* **16**, 734 (2020).
- [5] K. M. Bastiaans, D. Chatzopoulos, J.-F. Ge, D. Cho, W. O. Tromp, J. M. van Ruitenbeek, M. H. Fischer, P. J. de Visser, D. J. Thoen, E. F. C. Driessen, T. M. Klapwijk, and M. P. Allan, Direct evidence for Cooper pairing without a spectral gap in a disordered superconductor above T_c , *Science* **374**, 608 (2021).
- [6] L. Grünhaupt, M. Spiecker, D. Gusenkova, N. Maleeva, S. T. Skacel, I. Takmakov, F. Valenti, P. Winkel, H. Rotzinger, W. Wernsdorfer, A. V. Ustinov, and I. M. Pop, Granular aluminium as a superconducting material for high-impedance quantum circuits, *Nature Materials* **18**, 816 (2019).
- [7] M. Esposito, A. Ranadive, L. Planat, and N. Roch, Perspective on traveling wave microwave parametric amplifiers, *Applied Physics Letters* **119**, 120501 (2021).
- [8] P. K. Day, H. G. LeDuc, B. A. Mazin, A. Vayonakis, and J. Zmuidzinas, A broadband superconducting detector suitable for use in large arrays, *Nature* **425**, 817 (2003).
- [9] G. N. Gol'tsman, O. Okunev, G. Chulkova, A. Lipatov, A. Semenov, K. Smirnov, B. Voronov, A. Dzardanov, C. Williams, and R. Sobolewski, Picosecond superconducting single-photon optical detector, *Applied Physics Letters* **79**, 705 (2001).
- [10] K. Kouwenhoven, I. Elwakil, J. van Wingerden, V. Murugesan, D. J. Thoen, J. J. A. Baselmans, and P. J. de Visser, Model and Measurements of an Optical Stack for Broadband Visible to Near-Infrared Absorption in TiN MKIDs, *Journal of Low Temperature Physics* **209**, 1249 (2022).
- [11] R. Ma, Q. Huan, J. Huang, X. Zhang, Y. Xiao, H. Xu, H. Han, X. Liu, W. Peng, H. Li, X. Zhang, and L. You, Disorder enhanced relative intrinsic detection efficiency in NbTiN superconducting nanowire single photon detectors at high temperature, *Applied Physics Letters* **124**, 072601 (2024).
- [12] H. G. LeDuc, B. Bumble, P. K. Day, B. H. Eom, J. Gao, S. Golwala, B. A. Mazin, S. McHugh, A. Merrill, D. C. Moore, O. Noroozian, A. D. Turner, and J. Zmuidzinas, Titanium nitride films for ultrasensitive microresonator detectors, *Applied Physics Letters* **97**, 102509 (2010).
- [13] M. Sidorova, A. D. Semenov, I. Charaev, M. Gonzalez, A. Schilling, S. Gyger, and S. Steinhauer, Phonon heat capacity and disorder: New opportunities for performance enhancement of superconducting devices (2023), arXiv:2308.12090 [cond-mat].
- [14] J. M. Martinis, Saving superconducting quantum processors from decay and correlated errors generated by gamma and cosmic rays, *npj Quantum Information* **7**, 1 (2021).
- [15] R.-P. Riwar and G. Catelani, Efficient quasiparticle traps with low dissipation through gap engineering, *Physical Review B* **100**, 144514 (2019).
- [16] K. Karatsu, A. Endo, J. Bueno, P. J. de Visser, R. Barends, D. J. Thoen, V. Murugesan, N. Tomita, and J. J. A. Baselmans, Mitigation of cosmic ray effect on microwave kinetic inductance detector arrays, *Applied Physics Letters* **114**, 032601 (2019).
- [17] J. J. A. Baselmans, S. J. C. Yates, P. Diener, and P. J. de Visser, Ultra Low Background Cryogenic Test Facility for Far-Infrared Radiation Detectors, *Journal of Low Temperature Physics* **167**, 360 (2012).
- [18] L. Cardani, F. Valenti, N. Casali, G. Catelani, T. Charpentier, M. Clemenza, I. Colantoni, A. Cruciani, G. D'Imperio, L. Gironi, L. Grünhaupt, D. Gusenkova, F. Henriques, M. Lagoin, M. Martinez, G. Pettinari, C. Rusconi, O. Sander, C. Tomei, A. V. Ustinov, M. Weber, W. Wernsdorfer, M. Vignati, S. Pirro, and I. M. Pop, Reducing the impact of radioactivity on quantum circuits in a deep-underground facility, *Nature Communications* **12**, 2733 (2021).
- [19] P. J. de Visser, D. J. Goldie, P. Diener, S. Withington, J. J. A. Baselmans, and T. M. Klapwijk, Evidence of a Nonequilibrium Distribution of Quasiparticles in the Microwave Response of a Superconducting Aluminum Resonator, *Physical Review Letters* **112**, 047004 (2014).
- [20] A. P. Vepsäläinen, A. H. Karamlou, J. L. Orrell, A. S. Dogra, B. Loer, F. Vasconcelos, D. K. Kim, A. J. Melville, B. M. Niedzielski, J. L. Yoder, S. Gustavsson, J. A. Formaggio, B. A. VanDevender, and W. D. Oliver, Impact of ionizing radiation on superconducting qubit coherence, *Nature* **584**, 551 (2020).
- [21] R. Barends, J. Wenner, M. Lenander, Y. Chen, R. C. Bialczak, J. Kelly, E. Lucero, P. O'Malley, M. Mariantoni, D. Sank, H. Wang, T. C. White, Y. Yin, J. Zhao, A. N. Cleland, J. M. Martinis, and J. J. A. Baselmans, Minimizing quasiparticle generation from stray infrared light in superconducting quantum circuits, *Applied Physics Letters* **99**, 113507 (2011).
- [22] A. V. Sergeev and M. Yu. Reizer, Photoresponse mechanisms of thin superconducting films and superconducting detectors, *International Journal of Modern Physics B* **10**, 635 (1996).
- [23] R. Barends, S. van Vliet, J. J. A. Baselmans, S. J. C. Yates, J. R. Gao, and T. M. Klapwijk, Enhancement of quasiparticle recombination in Ta and Al superconductors by implantation of magnetic and nonmagnetic atoms, *Physical Review B* **79**, 020509(R) (2009).
- [24] L. Grünhaupt, N. Maleeva, S. T. Skacel, M. Calvo, F. Levy-Bertrand, A. V. Ustinov, H. Rotzinger, A. Monfardini, G. Catelani, and I. M. Pop, Loss Mechanisms and Quasiparticle Dynamics in Superconducting Microwave Resonators

Made of Thin-Film Granular Aluminum, *Physical Review Letters* **121**, 117001 (2018).

- [25] A. G. Moshe, E. Farber, and G. Deutscher, Granular superconductors for high kinetic inductance and low loss quantum devices, *Applied Physics Letters* **117**, 062601 (2020).
- [26] S. B. Kaplan, C. C. Chi, D. N. Langenberg, J. J. Chang, S. Jafarey, and D. J. Scalapino, Quasiparticle and phonon lifetimes in superconductors, *Physical Review B* **14**, 4854 (1976).
- [27] M. Y. Reizer and A. V. Sergeev, Electron-phonon interaction in impure metals and superconductors, *Zh. Eksp. Teor. Fiz.* **90**, 1056 (1986).
- [28] T. P. Devereaux and D. Belitz, Quasiparticle inelastic lifetimes in disordered superconducting films, *Physical Review B* **44**, 4587 (1991).
- [29] M. H. Read and C. Altman, A new structure in tantalum thin films, *Applied Physics Letters* **7**, 51 (1965).
- [30] C. M. Wilson and D. E. Prober, Quasiparticle number fluctuations in superconductors, *Physical Review B* **69**, 094524 (2004).
- [31] M. Reizer, Electron-electron relaxation in two-dimensional impure superconductors, *Physical Review B* **61**, 7108 (2000).
- [32] A. Rothwarf and B. N. Taylor, Measurement of Recombination Lifetimes in Superconductors, *Physical Review Letters* **19**, 27 (1967).
- [33] S. B. Kaplan, Acoustic matching of superconducting films to substrates, *Journal of Low Temperature Physics* **37**, 343 (1979).
- [34] W. Eisenmenger, K. Laßmann, H. J. Trumpp, and R. Krauß, Quasiparticle recombination and 2Δ -phonon-trapping in superconducting tunneling junctions, *Applied physics* **11**, 307 (1976).
- [35] S. A. H. de Rooij, J. J. A. Baselmans, V. Murugesan, D. J. Thoen, and P. J. de Visser, Strong reduction of quasiparticle fluctuations in a superconductor due to decoupling of the quasiparticle number and lifetime, *Physical Review B* **104**, L180506 (2021).
- [36] A. Sergeev and V. Mitin, Electron-phonon interaction in disordered conductors: Static and vibrating scattering potentials, *Physical Review B* **61**, 6041 (2000).
- [37] D. C. Mattis and J. Bardeen, Theory of the Anomalous Skin Effect in Normal and Superconducting Metals, *Physical Review* **111**, 412 (1958).
- [38] J. Gao, J. Zmuidzinas, A. Vayonakis, P. Day, B. Mazin, and H. Leduc, Equivalence of the Effects on the Complex Conductivity of Superconductor due to Temperature Change and External Pair Breaking, *Journal of Low Temperature Physics* **151**, 557 (2008).
- [39] P. J. de Visser, J. J. A. Baselmans, P. Diener, S. J. C. Yates, A. Endo, and T. M. Klapwijk, Number Fluctuations of Sparse Quasiparticles in a Superconductor, *Physical Review Letters* **106**, 167004 (2011).
- [40] P. C. J. J. Coumou, M. R. Zwaard, E. F. C. Driessen, P. J. de Visser, J. J. A. Baselmans, and T. M. Klapwijk, Microwave Properties of Superconducting Atomic-Layer Deposited TiN Films, *IEEE Transactions on Applied Superconductivity* **23**, 7500404 (2013).
- [41] A. G. Kozorezov, A. A. Golubov, J. K. Wigmore, D. Martin, P. Verhoeve, R. A. Hijmering, and I. Jerjen, Inelastic scattering of quasiparticles in a superconductor with magnetic impurities, *Physical Review B* **78**, 174501 (2008).
- [42] A. Pippard, CXXII. Ultrasonic attenuation in metals, *The London, Edinburgh, and Dublin Philosophical Magazine and Journal of Science* **46**, 1104 (1955).
- [43] M. A. Skvortsov and M. V. Feigel'man, Subgap states in disordered superconductors, *Journal of Experimental and Theoretical Physics* **117**, 487 (2013).
- [44] B. Sacépé, C. Chapelier, T. I. Baturina, V. M. Vinokur, M. R. Baklanov, and M. Sanquer, Disorder-Induced Inhomogeneities of the Superconducting State Close to the Superconductor-Insulator Transition, *Physical Review Letters* **101**, 157006 (2008).
- [45] A. A. Abrikosov and L. P. Gor'kov, *Zh. Eksp. Teor. Fiz.* **39**, 1781 (1960).
- [46] A. I. Kardakova, P. C. J. J. Coumou, M. I. Finkel, D. V. Morozov, P. P. An, G. N. Goltsman, and T. M. Klapwijk, Electron-Phonon Energy Relaxation Time in Thin Strongly Disordered Titanium Nitride Films, *IEEE Transactions on Applied Superconductivity* **25**, 1 (2015).
- [47] D. J. Thoen, B. G. C. Bos, E. A. F. Haalebos, T. M. Klapwijk, J. J. A. Baselmans, and A. Endo, Superconducting NbTiN Thin Films With Highly Uniform Properties Over a 100 mm Wafer, *IEEE Transactions on Applied Superconductivity* **27**, 1 (2017).
- [48] J. Gao, M. Daal, A. Vayonakis, S. Kumar, J. Zmuidzinas, B. Sadoulet, B. A. Mazin, P. K. Day, and H. G. Leduc, Experimental evidence for a surface distribution of two-level systems in superconducting lithographed microwave resonators, *Applied Physics Letters* **92**, 152505 (2008).
- [49] G. Abadias, J. J. Colin, D. Tingaud, Ph. Djemia, L. Belliard, and C. Tromas, Elastic properties of α - and β -tantalum thin films, *Thin Solid Films* **688**, 137403 (2019).
- [50] P. J. de Visser, *Quasiparticle Dynamics in Aluminium Superconducting Microwave Resonators*, Ph.D. thesis, Delft University of Technology, Delft (2014).
- [51] B. Keck and A. Schmid, Superconductivity and electron-phonon interaction in impure simple metals, *Journal of Low Temperature Physics* **24**, 611 (1976).
- [52] A. Schmid, On the dynamics of electrons in an impure metal, *Zeitschrift für Physik* **271**, 251 (1974).
- [53] C. Kittel, *Quantum Theory of Solids* (Wiley, 1987).
- [54] T. Kühn, D. V. Anghel, J. P. Pekola, M. Manninen, and Y. M. Galperin, Heat transport in ultrathin dielectric membranes and bridges, *Physical Review B* **70**, 125425 (2004).
- [55] K. Petersen, Silicon as a mechanical material, *Proceedings of the IEEE* **70**, 420 (1982).

- [56] P. J. de Visser, S. A. de Rooij, V. Murugesan, D. J. Thoen, and J. J. Baselmans, Phonon-Trapping-Enhanced Energy Resolution in Superconducting Single-Photon Detectors, *Physical Review Applied* **16**, 034051 (2021), arXiv:2103.06723.
- [57] L. D. Landau and E. M. Lifshitz, *Statistical Physics: Volume 5* (Elsevier, 2013).
- [58] C. N. Thomas, S. Withington, and D. J. Goldie, Electrothermal model of kinetic inductance detectors, *Superconductor Science and Technology* **28**, 045012 (2015).
- [59] E. M. Gershenzon, Electron-phonon interaction in ultrathin Nb films, *Zh. Eksp. Teor. Fiz.* **97**, 901 (1990).
- [60] P. H. Kes and C. C. Tsuei, Two-dimensional collective flux pinning, defects, and structural relaxation in amorphous superconducting films, *Physical Review B* **28**, 5126 (1983).
- [61] M. Tinkham, *Introduction to Superconductivity* (Dover Publications, 2004).
- [62] M. Magnuson, G. Greczynski, F. Eriksson, L. Hultman, and H. Högberg, Electronic structure of β -Ta films from X-ray photoelectron spectroscopy and first-principles calculations, *Applied Surface Science* **470**, 607 (2019).
- [63] E. F. C. Driessen, P. C. J. J. Coumou, R. R. Tromp, P. J. de Visser, and T. M. Klapwijk, Strongly Disordered TiN and NbTiN s-Wave Superconductors Probed by Microwave Electrodynamics, *Physical Review Letters* **109**, 107003 (2012).
- [64] A. V. Khvalyuk, T. Charpentier, N. Roch, B. Sacépé, and M. V. Feigel'man, Near power-law temperature dependence of the superfluid stiffness in strongly disordered superconductors, *Physical Review B* **109**, 144501 (2024).
- [65] A. Kardakova, M. Finkel, D. Morozov, V. Kovalyuk, P. An, C. Dunscombe, M. Tarkhov, P. Mauskopf, T. M. Klapwijk, and G. Goltsman, The electron-phonon relaxation time in thin superconducting titanium nitride films, *Applied Physics Letters* **103**, 252602 (2013).
- [66] K. Hansen, M. Cardona, A. Dutta, and C. Yang, Plasma Enhanced Atomic Layer Deposition of Plasmonic TiN Ultrathin Films Using TDMATi and NH₃, *Materials* **13**, 1058 (2020).
- [67] D. Chen, J. Chen, Y. Zhao, B. Yu, C. Wang, and D. Shi, Theoretical study of the elastic properties of titanium nitride, *Acta Metallurgica Sinica (English Letters)* **22**, 146 (2009).
- [68] M. Sidorova, A. Semenov, H.-W. Hübers, K. Ilin, M. Siegel, I. Charaev, M. Moshkova, N. Kaurova, G. N. Goltsman, X. Zhang, and A. Schilling, Electron energy relaxation in disordered superconducting NbN films, *Physical Review B* **102**, 054501 (2020).
- [69] K. S. Il'in, N. G. Ptitsina, A. V. Sergeev, G. N. Gol'tsman, E. M. Gershenzon, B. S. Karasik, E. V. Pechen, and S. I. Krasnosvobodtsev, Interrelation of resistivity and inelastic electron-phonon scattering rate in impure NbC films, *Physical Review B* **57**, 15623 (1998).